This document is confidential and is proprietary to the American Chemical Society and its authors. Do not copy or disclose without written permission. If you have received this item in error, notify the sender and delete all copies.

Stochastic Ionic Transport in Single Atomic Zero-D Pores

Journal:	ACS Nano
Manuscript ID	nn-2020-047165.R1
Manuscript Type:	Article
Date Submitted by the Author:	n/a
Complete List of Authors:	Thiruraman, Jothi Priyanka; University of Pennsylvania School of Engineering and Applied Science, ESE Masih Das, Paul; University of Pennsylvania, Physics and Astronomy Drndic, Marija; University of Pennsylvania, Physics and Astronomy



Stochastic Ionic Transport in Single Atomic

Zero-D Pores

Jothi Priyanka Thiruraman^{1,2}, Paul Masih Das¹, Marija Drndić¹*

¹Department of Physics and Astronomy, and ²Department of Electrical and Systems Engineering,
University of Pennsylvania, Philadelphia, Pennsylvania, 19104, USA

*Corresponding author: drndic@physics.upenn.edu.

Abstract

We report on single atomic, zero-dimensional (zero-D) pores fabricated using aberration corrected-scanning transmission electron microscopy (AC-STEM) in monolayer MoS_2 . Pores are comprised of a few atoms missing in the 2D lattice (1- 5 Mo atoms) of characteristic sizes ~ 0.5 nm to 1.2 nm, and pore edges directly probed by AC-STEM to map the atomic structure. We categorize them into ~ 30 geometrically possible zigzag, armchair and mixed configurations. While theoretical studies predict that transport properties of 2D pores in this size range depend strongly on pore size and their atomic configuration, Zero-D pores show an average conductance in the range of ~ 0.8 nS (bias up to 0.1 V), similar to biological pores. Furthermore, current-voltage (I-V) characteristics are largely independent of bulk molarity (10 mM to 3 M KCl) and the type of cation (K⁺, Li⁺, Mg⁺⁺). This work lays the experimental foundation for understanding of confinement effects possible in atomic-scale 2D material pores and the realization of solid-state analogues of ion channels in biology.

Keywords

Zero-D pore, atomic pore, angstrom-size pore, sub-nm pore, nanopore, ionic current, molybdenum disulfide, 2D material, transition metal dichalcogenides.

In the recent years, biological proteins such as Na⁺ channels, K⁺ channels and aquaporins are being revered as touchstones for their water molecule and ionic transport properties. Studies have shown unique non-linear current-voltage (I-V) characteristics in sub-nm solid-state pores fabricated and tuned under a variety of operating conditions. 1-5 These observations constitute a breakthrough in understanding water purification and ionic selectivity with low-dimensional materials. Among reports on fabrication using novel solid-state materials, there have been a few innovative device architectures that mimic biological protein ion channels such as K⁺ channels. For example, carbon nanotubes (CNTs) with 0.8-1.5 nm diameters, ^{6,7} nanocapillaries with 0.6 nm heights, 8,9 and nanopores in graphene, MoS₂, and WS₂ with ~ 0.2 nm to few-nm diameters, 4,10,11 have shown cation selectivity. Arrays of pores with diameters comparable to the hydrated ion sizes have been demonstrated in two-dimensional (2D) materials, opening a regime of transport studies at the atomic scale.^{2,4,12} A few notable experimental studies were conducted on single sub-1-nmdiameter 2D pores. 5,12 Here they used theoretical fits of conductance vs. pore diameter to quote the "experimental" 2D pore diameter in the sub-nm regime from measured currents^{2,5} rather than measure it directly, assuming that models are correct in the sub-nm regime. These pore diameter values were then used as important ingredients to obtain, what could be considered, a "by-design" match with theories² such as claiming evidence for "Coulomb blockade"⁵ and "atom-by-atom" pore formation phenomena. 13 However, the fabrication and ionic transport properties of *individual* atomically-engineered pores in 2D membranes is yet to be experimentally established.^{5,12} Effects arising from ion confinement such as quantized ionic conductance vs. pore diameter, Coulomb blockade and steric hindrance where the drop in conductance as successive hydration shells are prevented from passing through the small pores have been anticipated.^{4,5,14–17} Other competing effects may include hydrophobicity of pores. 18,19 Understanding ionic conduction phenomena in these confined geometries will expand their applications in drug delivery, biomedical, water filtration, nanopower generation and energy harvesting. 2,4,10,20,21,22

In this study, we create single atomic (sub-nm) pores in a monolayer 2D material, obtain their single-atom-resolution structural images, and probe the correlated current-voltage behavior in salt solutions. We fabricate devices with individual atomically-precise MoS_2 pores using aberration-corrected scanning transmission electron microscopy (AC-STEM). The resulting pores contain 1 to 5 missing Mo atoms with effective diameters (d_{TEM} , see *Methods* for definition and discussion) ranging from ~ 0.53 to 0.92 nm. Using atomic resolution images, we also present a

library of predicted MoS_2 pores with discretized sub-nm diameters and zigzag-armchair edge configurations. These pores constitute quasi-zero-dimensional (zero-D) channels^{5,12,14} with feature sizes comparable to the dimensions of water molecules (~ 0.3 nm), hydrated ions (~ 0.7 nm to 1 nm) and Debye screening lengths (~ 0.1 nm to 3 nm in 3 M to 10 mM KCl, respectively).^{5,23,24}

Using ionic transport measurements, the wetting properties, ion current noise, and conductivity properties of individual zero-D MoS₂ pores are characterized. We present a methodology for inducing a conducting ion channel in a sub-nm 2D pore using ethanol solutions and probe different ionic states (un-wet, partially wet, and fully wet) through current-voltage and noise power spectral density measurements. Due to their similar effective sizes, the measured conductance (G) range for zero-D pores (0.6 nS - 1 nS) in monolayer MoS₂ is similar to the conductance in biological ion channels. In the low-bias regime (± 100 mV), we also observe that the ionic conductivity of zero-D MoS₂ pores is largely independent of the bulk conductivity of different salt solutions and concentrations, making the pore almost equally conducting in 0.01 M KCl as in 3 M KCl. This is in contrast to larger-diameter pores in the same material where pore and bulk conductivity are approximately the same.^{25,26} These experimental findings are overall consistent with molecular dynamics simulations of sub-5 nm MoS₂ nanopores for 1 M KCl²⁷ and provide opportunities for further studies on low-dimensional ionic transport in solid state materials.

Results and Discussion

Pore fabrication²⁸ in 2D materials has been realized using several methods including electron^{29,30} and ion irradiation,³¹ electroporation,^{13,32} polymer patterning,^{33,34} annealing/healing³⁵ *in-situ* transmission electron microscopy (TEM),³⁶ and plasma etching.^{10,28,37} Electron beam drilling with sub-nm size probes enables the formation of individual pores while offering control over pore size and geometry. With the growing use of aberration-corrected electron optics, transmission electron beams can be focus to diameters < 0.1 nm and have enabled studies of 2D materials down to an unprecedented resolution of \sim 39 pm.³⁸ Recent advancements in electron microscopy also open possibilities for precise nanopore device engineering in 2D materials: to controllably make single and few-atom-sized pores and to atomically control the pore edges. Defect and pore creation in 2D materials has been studied in vacuum inside the TEM ^{39–44}, where 2D flakes typically hang off the supporting substrate or TEM grid and the chip is not designed for *ex situ* nanofluidics. Correlating advanced microscopy (AC-TEM) insights with transport properties from the same 2D devices measured *ex situ* has been challenging due to device

requirements, such as having a single nanopore within an otherwise continuous membrane that does not leak, and a nanopore that is sufficiently stable in liquid or gas environments.

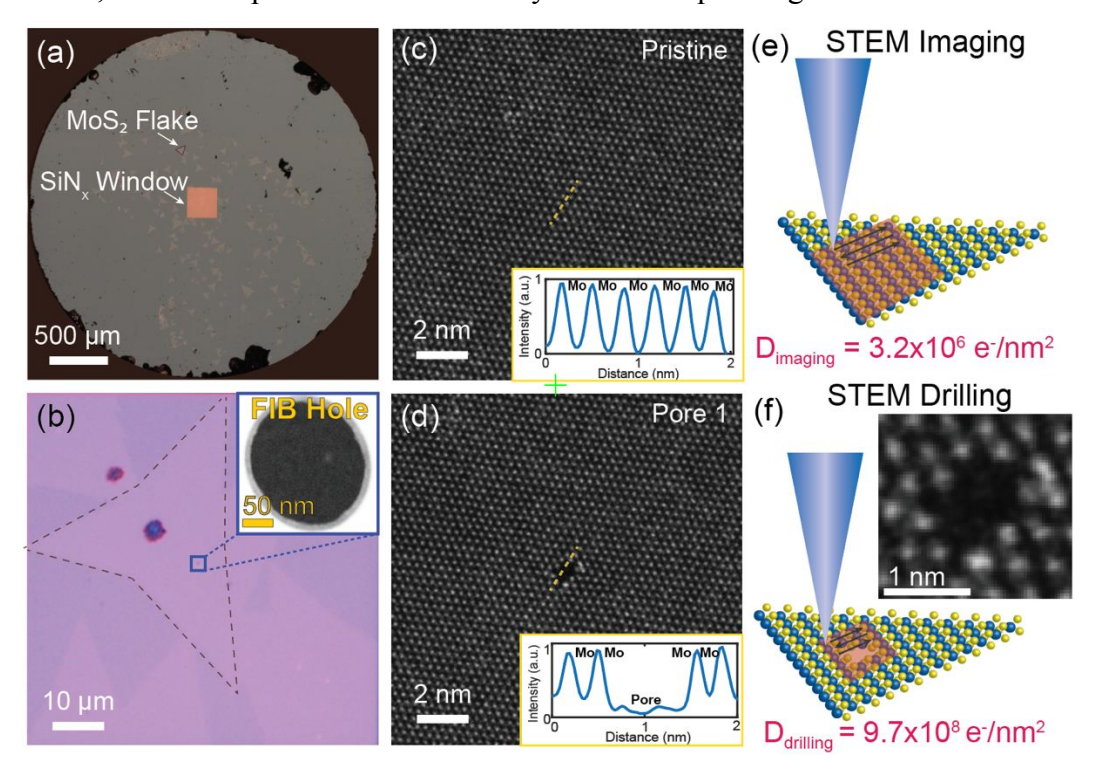


Figure 1. Selected area AC-STEM drilling for individual sub-nm MoS₂ pores. (a) Optical image of a 3-mm-diameter SiN_x/Si circular chip platform (grey) for the TEM-beam fabrication of sub-nm pores with transferred MoS₂ flakes. (b) A monolayer MoS₂ flake (outlined by the purple dashed lines) transferred over a ~ 150- 200 nm-diameter focused ion beam hole on a SiN_x/Si chip (inside the blue square) and annealed to form a seal with the supporting chip. 45 Inset: Zoom in TEM image of the FIB hole with suspended MoS₂ flake (c) Atomic resolution image of pristine (as-grown and transferred) monolayer MoS₂ suspended on a SiN_x/Si chip and (d) the lattice with a pore of effective diameter (d_{TEM} , see *Methods* for definition) ~ 1.1 nm. Z contrast is indicative of Mo and S atoms. (e) Schematic showing imaging of suspended monolayer MoS₂ under an aberration-corrected scanning transmission electron (AC-STEM) beam (light blue) with a dose of 3.2×10^6 e-/nm². Mo and S atoms are shown in dark blue and yellow, respectively, while the electron exposure area is shown in orange. (f) Illustration of the sub-nm pore drilling using STEM selected area exposure technique with a dose of 9.7×10^8 e-/nm² and (inset) a completely drilled zero-D pore.

Atomic pore fabrication. Figure 1 shows the sub-nm diameter MoS₂ pore fabrication process using aberration-corrected scanning transmission electron microscope (STEM) selected-area

exposure of the 2D membrane. A monolayer MoS_2 flake is transferred onto a $50 \times 50 \,\mu\text{m}^2$ window in the center of the 3 mm diameter TEM grid with a 30 nm thick SiN_x film on top of a 290- μ m-thick Si support substrate (**Figure 1(a)**). As indicated in the inset of **Figure 1(b)**, the electron transparent SiN_x window contains a ~ 150 nm diameter hole drilled with a focused Ga^+ ion beam (FIB). The MoS_2 flake ~ 50 to 80 μ m in size is positioned such that it is suspended over the FIB hole (**Figure 1(b)**) and annealed at 300°C with Ar:H₂. The pore drilling process starts by zooming into the suspended MoS_2 region covering the FIB hole to acquire a high-angle annular dark-field (HAADF) image (dose = 3.2×10^6 e-/nm², time = 8 s) of the pristine (as-grown and transferred) lattice (**Figure 1(c)**).

For a 2D material exposed to an electron beam, defect production is mediated by momentum transfer from energetic electrons to lattice atoms (knock-on damage) and in-plane electronic excitations (radiolysis). Here, we employ a STEM acceleration voltage of 80 kV, in which the maximum knock-on electron energy transfer is lower than the displacement thresholds for Mo (20 eV) and S (6.5 eV) atoms in monolayer MoS_2 . Previous reports have also demonstrated that an exposure dose of $\sim 10^6$ e-/nm² causes negligible radiolysis damage in monolayer MoS_2 . At an area) to selected area (1 nm × 1 nm area) exposure, in which the raster area of the electron beam is reduced, thereby increasing the dose to 9.7×10^8 e-/ nm² (total exposure time = 10 s). At this exposure dose, radiolysis causes atoms to be sputtered off the lattice within the selected area, thus creating a sub-nm pore (Pore 1, **Figure 1(d)**). The process is demonstrated schematically in **Figures 1(e)-(f)**. Atomic pores are formed by removing a fixed, small number of Mo and S atoms, with edges that mainly follow the lattice shape.

Compared to other electron exposure techniques such as high-resolution TEM (HRTEM) drilling and electron beam lithography, the use of a highly focused (probe beam with full width at half maximum (FWHM) ~ 0.1 nm) STEM beam allows for simultaneous imaging and atom removal while creating pores with atomically precise geometries. The resulting electron micrographs of the zero-D pore are crucial in accurately characterizing pore size and atomic structure for subsequent ionic transport measurements.

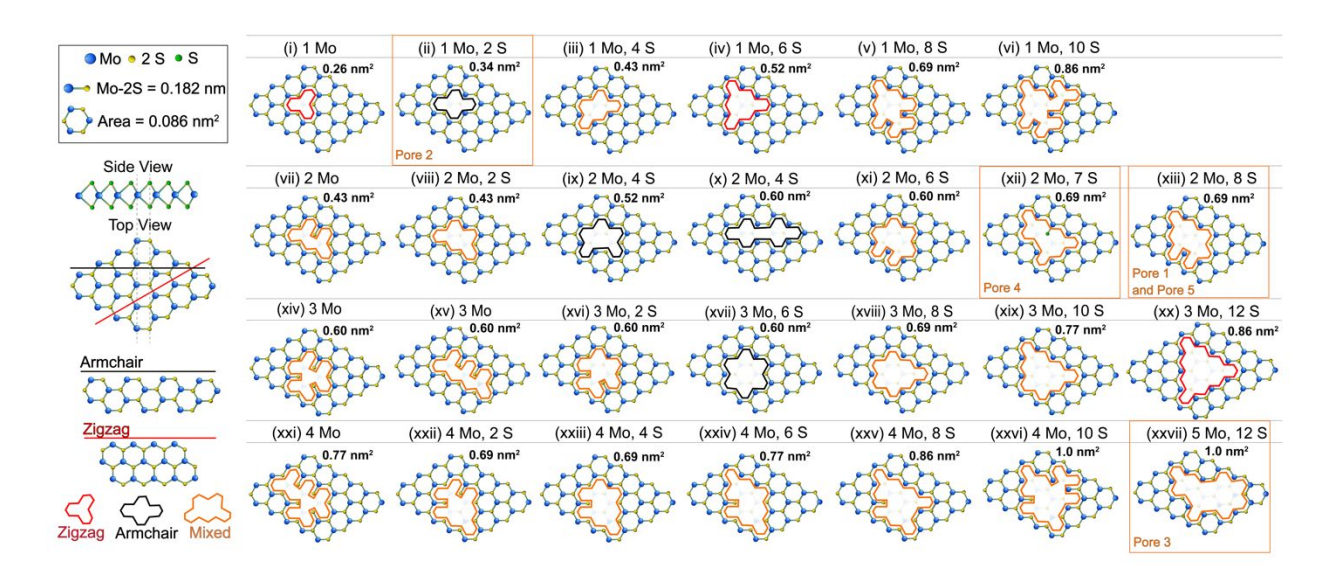


Table 1. Atomic pore models. Illustration of geometrically possible configurations of MoS_2 atomic (zero-D) pores with areas ≤ 1 nm². Red and black pore edges correspond to zigzag and armchair edge configurations, respectively, and in orange are shown the mixed pore edges that are a combination of zigzag and armchair. The pore areas are approximately equal to the multiples of the area of a unit ring, 0.086 nm², comprised of 3 Mo and 6 S atoms, illustrated on the top left. These geometrical pore models assume perfect pore edges following the shape of the lattice, and their thermodynamic stability in vacuum and ionic solutions is not *a priori* guaranteed.

Geometric pore models and atomic structures of fabricated pores. Selected area STEM drilling enables fabrication and investigation of a finite number of pores fabricated with an area below 1 nm². Molecular dynamics modeling has shown how the pore edge configuration in a 2D material drastically affects its molecular transport. For example, Heiranian *et al.* theoretically predicted that a nanopore with only Mo-terminated edges allows for higher water fluxes compared to pores that are mixed (*i.e.*, edges with Mo and S atoms), S-terminated pores, and C-terminated (*i.e.*, graphene) pores. We first present a library of 27 geometrically possible combinations of missing atoms to create zero-D MoS₂ pores, ≤ 1 nm² in area. These pore model configurations are shown in **Table 1** and correspond to 1 to 5 Mo atoms missing, and up to 12 S atoms missing. Pore areas range from (i) $A_{\text{model}} \sim 0.26$ nm² for missing 1 Mo atom, to (xxvii) $A_{\text{model}} \sim 1.0$ nm² for missing 5 Mo and 12 S atoms.

The geometric models provided in **Table 1** are labeled as (n Mo, m S) and defined by (n, m), where n and m are the numbers of missing Mo and S atoms, respectively. These models show ideal pores without lattice distortions around the pore edges that we can occasionally observe in

experiments. For example, in the image of Pore 1 in **Figure 1(f)**, we observe about 3 to 4 Mo atoms that have been displaced at the upper right side of the pore's edge. The specific pore models (i), (vii), (xiv), (xxi) have only Mo atoms missing and are simply labeled as (1 Mo) to (4 Mo). To compute pore sizes, the area of one hexagonal ring, $A_{\text{ring, Model}} = 0.086 \text{ nm}^2$ (**Table 1,** *Top View* of the lattice) is estimated from the normal distance from the Mo atom to the line connecting the two S atoms, a distance of 0.182 nm.^{4,27} For each model, the pore area is estimated from the number of missing hexagonal rings. For example, for pore (i) (1 Mo), $A_{\text{(1Mo), Model}} = n_r * A_{\text{ring, Model}} = 0.26 \text{ nm}^2$ where the number of missing rings is $n_r = 3$.

Since STEM drilling preserves the localized atomic structure of the MoS₂, pore edges are combinations of zigzag and/or armchair paths, which are defined in **Table 1**. A few examples of purely *zigzag pores* are (i) (1 Mo) and (xx) (3 Mo, 12 S), while purely *armchair pores* include (x) (2 Mo, 4 S) and (xviii) (3 Mo, 6 S). Conventional descriptions of pore diameter applicable for nmscale pores breaks down since these pores can no longer be assumed circular (**Table 1**). A better way to capture the pore size and anisotropy is using the histogram of pore sizes in different planar directions passing through the pore's center of mass (See SI of Ref. 4).⁴ Here we use the number of missing Mo and S atoms along with a schematics of the most probable pore edge configuration and suggest to generalize this notation for similar 2D nanopore studies in the future.

While **Table 1** shows the most geometrically possible combinations of zero-D pores in a monolayer MoS₂ lattice with an area below 1 nm², it explicitly displays a few pore geometries that are likely feasible and can be fabricated through STEM drilling (such as in **Figure 1**). For example, *armchair pores* (ix) (2 Mo, 4 S) and (x) (2 Mo, 4 S) contain the same missing atoms of 2 Mo atoms and 4 S atoms, however, they are neither identical in their pore shape nor in area ((ix) 0.52 nm² and (x) 0.60 nm². Similarly, (xiv) 3 Mo and (xv) 3 Mo illustrate pores that are a combination of zigzag and armchair pore edges (*i.e.*, mixed) with the same theoretical area of 0.60 nm² but differ in their shape as seen in **Table 1**.

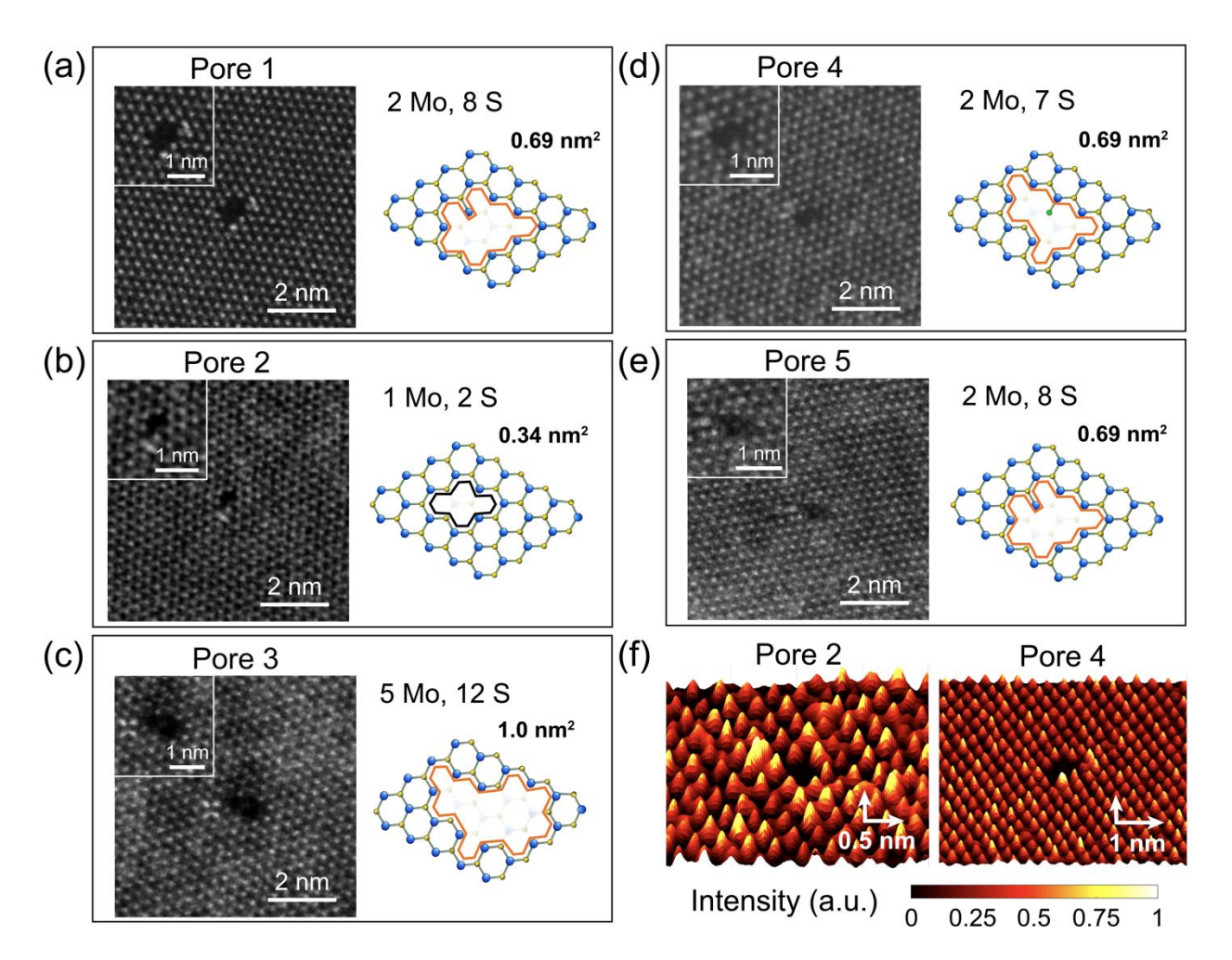


Figure 2. TEM images of MoS₂ (sub-nm-size) atomic pores and pore models. Zigzag-armchair zero-D pores in MoS₂. AC-STEM image (left) and schematic (right) of zero-D pores with (a) (2 Mo, 8 S), (b) (1 Mo, 2 S), (c) (5 Mo, 12 S), (d) (2 Mo, 7 S), and (e) (2 Mo, 8 S) atoms missing. (f) The 3-dimensional renderings of the intensity from the HAADF images of the pores shown in (b) and (d) are also provided.

In this case, we find that the pore in (xv) is difficult to experimentally fabricate and we attribute this to its highly elongated shape: under electron irradiation, pores prefer circular expansion due to the reduced displacement energy for atoms on the pore edge.⁴² More convoluted and intricate pore edges such as those depicted in (xxi), (xxii) pose a challenging fabrication and detection task even for tools with high controllability such as STEM due to the low displacement threshold and Z-contrast of chalcogen sites.^{31,39} Even more importantly, the structural stability of such artistically rendered, intricate pores are far from guaranteed, is likely lattice dependent, and yet to be explored and understood.

Atomic structure, formation and stability of 2D MoS₂ pores (as in pore configurations in **Table 1**) made by the electron beam irradiation in vacuum have been investigated using density functional theory (DFT), for example by Wang *et al.*⁴¹ who claimed that it is favorable for the ejected Mo atoms to attach to the 2D sheet, as well as by other authors who also modeled the ion conductance through 2D MoS₂ pores. ^{1,4,27} Ironically, many structural DFT stability simulations consider the material in vacuum. While these simulations seem suitable for TEM-only studies, their relevance is lower for nanofluidic devices where additional atoms and ions are present around the pore and can interact with the 2D material to form chemical bonds and even etch the material. ^{13,28,45} Stability of pores in salt solution is therefore a different and more complex problem than stability of pores in vacuum, as evidenced by various electrochemical phenomena observed between salt solutions and 2D materials such as oxidation. ^{13,28,45,49} There are exceptions of MoS₂ nanopore modeling in fluids, ^{1,4,27,22} but further work is required. DFT combined with molecular dynamics simulations may provide further insight, especially if they are in concordance with experimental findings. Our experiments outline several pores that were stable enough to be measured in ionic solutions.

Figure 2 demonstrates five example devices with AC-STEM HAADF images of zigzag and armchair structures successfully drilled and examined using the selected area technique shown in **Figure 1(c)-(f)**. The five pores include: (a) (2 Mo, 8 S), (b) (1 Mo, 2 S), (c) (5 Mo, 12 S), (d) (2 Mo, 7 S), and (e) (2 Mo, 8 S). Overall, the pores in this study range from 1–5 Mo vacancies with a pore area of 0.34 nm^2 to 1.0 nm^2 . Figure 2(f) shows 3D renderings of the intensity from the HAADF images of Pore 2 and Pore 4. The STEM beam can be controlled down to a $\sim 0.1 \text{ nm}$ probe size, nevertheless, the precision of this technique is limited due to sample drift and the relatively low displacement threshold ($\sim 7 \text{ eV}$) for S vacancies. 36,39 As a result of this, AC-STEM is mainly employed to create defects at Mo sites (Z = 42), while further efforts are needed to precisely control the composition of chalcogen (S) sites.

Pore contamination. It is likely to have 2D membrane and pore contamination by a carbon/graphitic film partially or completely covering the MoS₂ that cannot be easily observed in our HAADF images, as specifically discussed for similar MoS₂ films by Wen *et al.*⁵⁰, who demonstrated the detection of often-missed, lighter atoms (C, O, N) by 4D-STEM imaging. This additional material could alter the pore's wetting and other properties, reduce its diameter or

completely block the pore, and also yield smaller ionic current than predicted since the contaminated pore may be significantly thicker. For larger, nm-diameter MoS_2 pores, a good agreement was found between the ionic conductance models and expected $2D \, MoS_2$ pore thickness in the range $\sim 0.7 \, \text{nm}$ to $1.6 \, \text{nm}^{5,25}$, with the quoted device failure for 2 nm to 20-nm-diameter MoS_2 pores from membrane leakage ($G > 300 \, \text{nS}$) or pore clogging ($G < 10 \, \text{nS}$) of $< 30\%.^{25}$ Future efforts of modeling 2D pores and other ultrathin devices may wish to consider effects of carbon contamination, whose role is becoming increasingly more recognized and could be considered in interpreting behaviors of pores and devices at the atomic scale.

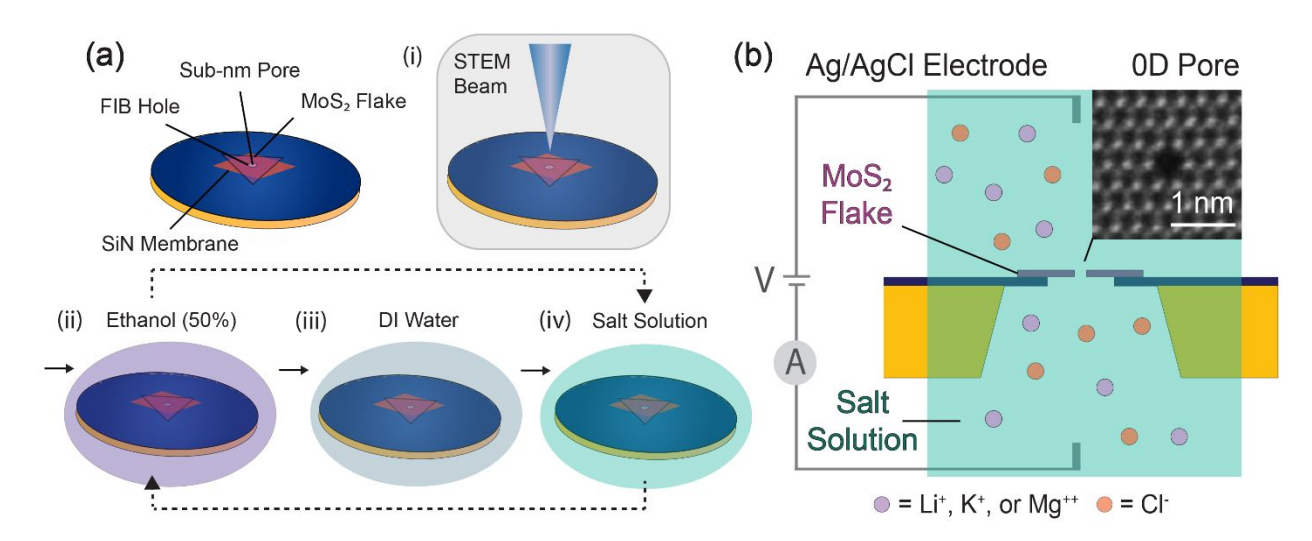


Figure 3. **Schematic of single pore STEM drilling, solution treatment, and measurement setup.** (a) Fabrication and pore wetting workflow for a suspended monolayer MoS₂ zero-D pore. (i) Drilling a sub-nm pore on the suspended MoS₂ flake. (ii) Wetting of pore with ethanol (50%) for 15-30 mins, (iii) Device rinsed in DI water before ionic measurement. (iv) Device flushed with salt solution for ionic measurement. (b) The design of nanopore ionic measurement consisting of a 2D MoS₂ nanopore separating two chambers of salt solution with Ag/AgCl electrodes (mounted on a microfluidic platform, not shown). (inset) A sample HAADF image of a sub-nm MoS₂ pore.

Ionic transport measurements and properties of single zero-D pores. After drilling in ultrahigh vacuum (p $\sim 1.7 \times 10^{-5} \text{ Pa}$) in the aberration corrected STEM, the zero-D pore is immediately stored in a vacuum-sealed container prior to experimental measurements to minimize oxidation-induced pore changes and expansion. ³³, ⁴⁵, ⁴⁷ **Figure 3(a)** displays a schematic of the 3 mm-diameter

 SiN_x/Si device (also pictured in **Figure 1(a)**) with a monolayer MoS_2 flake. The single zero-D pore that is drilled and imaged is located in the center of this membrane as explained previously in **Figure 1**. A number of studies have highlighted the importance of wetting nanochannels and pores prior to ionic measurements. ^{5,8} Here, we elaborate on the dedicated pre-treatment steps used to facilitate wetting of sub-nm MoS_2 pores while monitoring and examining intermediate responses before a measurable current state. We use a 1:1 mixture of ethanol and DI water to help wet our devices using the process shown schematically in **Figure 3(a)** (ii)-(iv). The process begins by immersing the device in the ethanol-water mixture for 15-30 minutes (**Figure 3(a)** (iii)). The following steps include rinsing with DI water and immersing the chip in salt solution (**Figure 3(a)** (iii)-(iv)). These last two steps take about one minute each with a total time of a few minutes. This cycle of processes is repeated sequentially a few times (about 3 to 6 times) until a detectable current (discussed later in **Figure 4**) is observed. Ionic transport measurements are performed with two-terminal Ag/AgCl electrodes (**Figure 3(b)**). The inset of **Figure 3(b)** shows an AC-STEM image of a pore which was not electrically measured. During measurements, we limit the applied voltage to ± 100 mV to minimize electric-field-induced damage to the device. ^{4,5}

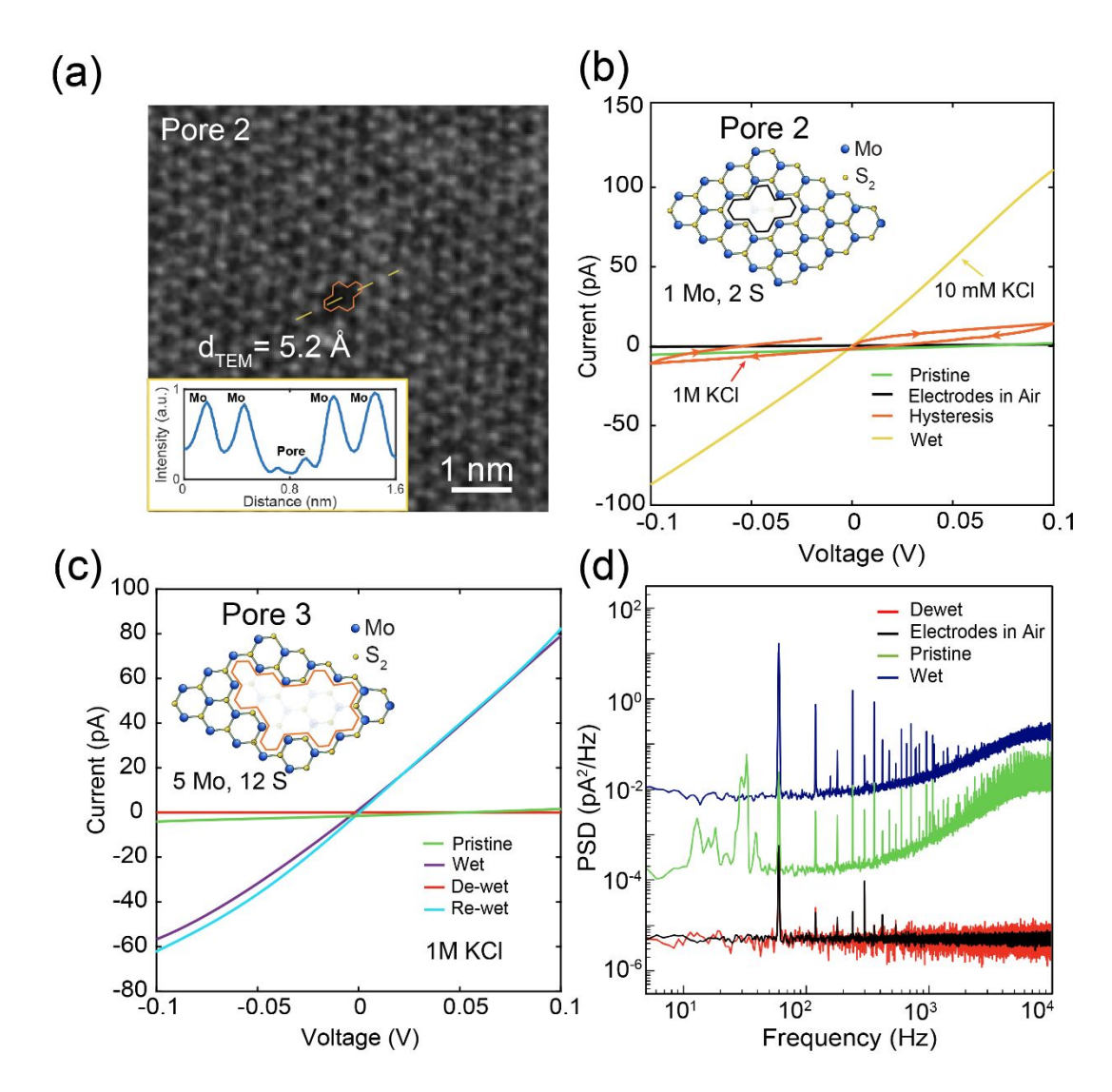


Figure 4. Ion current-voltage and noise curves in single pore devices. (a) AC-STEM image of the as-fabricated sub-nm Pore 2 (1 Mo, 2 S) in vacuum, prior to any I-V measurements with $d_{TEM} = 0.52$ nm. (b) Control and device I-V measurements: (black) bare Ag/AgCl electrodes in air, (orange) partially wet Pore 2, and (yellow) likely a fully wet Pore 2 after exposure to ethanol for 15 minutes. (c) I-V measurements of Pore 3 (5 Mo, 12 S) in 1 M KCl, pH 8.7 (purple) after 15 minutes ethanol exposure, (red) de-wetting after an additional 30 minutes in 1M KCl, and (blue) again after following the wetting procedure it was found to re-wet. For comparison, I-V curves for a pristine MoS_2 membrane are shown in green in both (b) and (c). (d) Current noise power spectral density (PSD) of samples in various conditions: (green) pristine membrane (no intentional holes), (black) bare Ag/AgCl electrodes in air, (red) a pore before ethanol wetting, and (blue) a pore after ethanol wetting.

We observe that the wetting of zero-D pores is a challenge for ionic measurements, indicating their hydrophobic nature. **Figure 4** represents two different sequence of events involved in wetting zero-D MoS₂ pores. The HAADF image of Pore 2 shown in **Figure 4(a)** indicates a structure with area of ~ 0.59 nm² ($d_{TEM} = \sqrt{\frac{4A_{TEM}}{\pi}} = 0.65$ nm), consisting of 1 Mo and 2 S atoms missing (also shown in **Table 1** as (ii)). The method to extract area from an HAADF images is shown in **Supplementary Figure S1.** The intensity profile of the dashed yellow line is shown in the inset of **Figure 4(a)** and demonstrates the absence of a single Mo atom in the periodic lattice structure. In the linescan across this pore, we also observe residual peaks whose intensity appears consistent with the presence of single S atoms. To better characterize and understand differences in conductance levels observed in a single zero-D pore sample (from vacuum to salt solution *via* ethanol immersion), we empirically categorize its observed transport behavior into three different states:

- (1) <u>State 1: Negligible conductance < 0.1 nS (~ 10 pA for V < 0.1 V) with I-V curves similar to those measured in pristine membranes in solution.</u> When pores were immersed in salt solution directly from vacuum, without any ethanol treatment, immeasurable ionic current was obtained (<10 pA in some cases), similar as the noise of the open circuit setup. This means that either (i) the ionic solution did not reach the pores (un-wet state) or that (ii) the ion current through these pores is below the detection limit. An example of this state is shown in red in **Figure 4(c)**.
- (2) <u>State 2: Measurable ionic current with pronounced hysteresis in I-V curves.</u> In this case, samples were immersed in ethanol prior to ionic measurements. The I-V curves were characterized by pronounced hysteresis but measurable signals. This is possibly due to incomplete pore wetting and gas molecules dissolved in solution and present on the surface of the microfluidic chip that make their way to the pore and affect the conductance. Hysteresis in I-V curves were noticed to be temporary in some devices before obtaining a conducting state (State 3). The orange curve in **Figure 4(b)** shows an example of State 2.
- (3) State 3: Measurable ionic current with no hysteresis in I-V curves. After immersing the samples for adequate (> 15 min) time in ethanol we observed I-V curves with no hysteresis corresponding to a measurable conductance up to ~ 0.8 nS. Such curves are shown in yellow in **Figure 4(b)** as well as purple and blue in **Figure 4(c)**. Additional examples of all three States can be found in **Supplementary Figure S3**.

Current-voltage characteristics of samples in this work show different scenarios with various sequences of events. Three of such sequences involving States 1-3 are shown for Pore 2 (**Figure 4(b)**), Pore 3 (**Figure 4(c)**) and Pore 4 (**Figure 5**), all successfully resulting in a measurable current and therefore ending in State 3. **Figure 4(b)** shows the first scenario where the ionic current-voltage curves obtained for Pore 2 go through the following stages in the wetting process: (i) after soaking in an ethanol:water mixture for 15 minutes (see Methods), we measure an I-V curve (orange) in 1 M KCl with hysteresis behavior where the maximum current is ± 10 pA. This value of current is comparable to pristine MoS₂ membranes with ethanol wetting (green) but shows a loop-like I-V curve characteristic of State 2, (ii) after placing the device into ethanol for 3 hours we measure in 10 mM KCl and observe an I-V curve (yellow) with $G \sim 0.98$ nS (*i.e.*, State 3).

We also have fabricated several pores which led to hysteresis-like I-V behavior and ended in State 2 (Pore 1 and Pore 5 shown in **Figure 1**) or had other issues such as excessive PMMA contamination. Pore/membrane breakage was observed in 3 devices which exhibited excessive conductance (~ 375 nS or higher, see **Supplementary Figure S3(a)**) caused likely due to (1) an unstable pore with significant PMMA contamination introduced during the transfer process. and (2) device damage during measurements. Out of a total of ~ 30 fabricated devices, 41% accounted for devices with drilled pores where ionic measurement was attempted. This also includes devices which had multiple sub-nm pores, for example Pores 6, 7 and 8 in **Supplementary Figure S3**. In the case of Pore 7 which was measured up to ± 0.5 V in 1 M KC, we observe a non-linear trend in I-V with a conductance $G \sim 2.2$ nS. In order to clearly distinguish between the background signal and signal from pore conduction, the control I-V curves for bare Ag/AgCl electrodes (black) and pristine MoS₂ membranes (green) were also measured (**Figure 4(b)**). As expected, the bare electrodes show a negligible conductance $G \sim 10$ pS with an ionic current of ~ 0.5 pA at -100 mV to 1 pA at +100 mV, also comparable to pristine membranes, $G \sim 10 - 30$ pS.

We do not detect any systematic dependence of conductance on pore size or geometry, but rather a stochastic set of values. For example, Pore 2 showed a higher conductance than Pore 3 despite smaller pore size recorded during TEM drilling and measurement at a lower KCl concentration (**Fig. 4b** *vs.* **Fig. 4c**). This may be a real, counterintuitive effect or it may be an artifact from pores changing during the course of the experiments. Previous non-equilibrium molecular dynamics (NEMD) conductance simulations on selected MoS₂ pore geometries

(including pores (ii) and (xix) from **Table 1**) showed that conductance varies in magnitude (~ 0.01 nS to ~ 1 nS) in this pore size range (~ 0.4 to 0.9 nm).^{4,27}

Sub-nm MoS₂ pore studies.^{1,4,5,13,27} It is useful to compare our findings with previous measurements. Single MoS₂ monolayer pores with somewhat larger diameters (1.1 nm and 1.4 nm, directly imaged by AC-TEM) yielded measured $G \sim 1.5$ nS and 10 nS in 1M KCl, respectively, and non-equilibrium molecular dynamic simulations for pores as in (ii) and (xix) in Table 1 computed $G \sim 0.02$ nS and $G \sim 0.03$ nS, respectively.⁴ Feng et al.⁵ reported conductance in pores made by electroporation to be ~ 1 nS (extracted at 100 mV) for quoted diameters of 0.3 nm, 0.6 nm, 0.8 nm and 1 nm,⁵ but failed to explain how pore diameters were obtained given that the pore images were not presented. Salt (bulk) conductivities are not directly applicable for sub-nm pores,²⁷ and a simple cylindrical pore model for conductance when used to gauge the size of electroporated pores¹³ is not sufficient. Up to \pm 5 V was applied (SI Figure S6 in Ref. ⁵) in 1 M KCl across a pore of presumably 0.3 nm in diameter (a single sulfur vacancy),⁵ while 0.8 V was previously found to be the critical voltage¹³ above which MoS₂ membrane can break. Single sulfur vacancies are common defects^{39,40} in "pristine" (i.e., membranes without intentional holes) MoS₂ membranes, but give negligible ionic conductance of pristine membranes, < 0.01 nS ⁴ (see also Figure 4), rather than 1 nS. These experimental details require attention in order to experimentally test and reproduce the far-reaching conclusions⁵ about a "voltage gap" for transport, the "signature" of "Coulomb Blockade", that increases as the pore diameter decreases. The "voltage gap" proportional to multiples of k_BT for which there is no transport, is not observed in our measurements of pores with well-characterized structure by AC-TEM, where we report the lowbias conductance consistent with the picture of reduced pore conductivity compared to bulk. Furthermore, authors claimed⁵ that soaking in ethanol, "30 min to 24 h to rule out hydrophobic effects", "eliminates the possibility that nonlinearity originates from hydrophobic effects".⁵ However, we find that while ethanol helps obtain measurable currents, we did not find that ethanol treatment alone guarantees that pores will be fully wet or that it eliminates hydrophobic effects and possible resulting nonlinearities in I-V curves. Theoretical simulations appear to miss this connection to experimental details (including pore contamination), 1,4,27,51 making the role of the alcohol-based wetting solvent unclear from an energy barrier standpoint which could elucidate its role in modification of the pore surfaces.

Reversible wetting-rewetting behavior. It is important to note that these conducting states are reversible in a sense that a conducting pore (State 3) can switch to a non-conducting state (State 1) (more discussion on hydrophobicity in pores is below). 18,19, 52-55 This implies that the ionic current paths may easily close in zero-D pores. We find that if the same pore is treated in ethanol again, it can start to show measurable ionic current and conduct (State 3). Ethanol is therefore critical for ionic measurements in 2D materials and especially for smaller-diameter zero-D pores here. This is demonstrated in Pore 3 (5 Mo, 12 S), which shows the second scenario where the pore was initially measured in State 1 after both 30 seconds and 5 minutes of ethanol wetting where we obtained an immeasurable and unstable I-V response. However, after an interval of 15 minutes in ethanol, the pore was observed to conduct (i.e., State 3) with $G \sim 0.73$ nS in 1 M KCl (purple curve in Figure 4(c)). This conducting state (~ 0.7 nS) was verified periodically after 10 minutes but was found to de-wet and reverted to State 1 after about 30 minutes after measuring in salt solution. This is denoted by the red I-V curve in Figure 4(c) with a max current of 0.9 pA at -100 mV and 0.6 pA at +100 mV. By repeating the wetting procedure, the pore was measured after 60 minutes, and was found to return to the conducting state 3 (light blue) with a conductance of 0.72 nS in 1M KCl. Later, this pore was stored in an ethanol mixture overnight and observed to still conduct after 14 hours with similar conductance values of 0.73 nS in 1 M KCl and 0.72 nS in 1 M LiCl.

Hydrophobic characteristics of single atomic pores. We observe that pores can wet and de-wet repeatedly, manifested by the fluctuation in the pore's conductance "on" and "off" upon successive current-voltage measurements, on the timescales of minutes. This resembles, at least qualitatively, the behavior of biological (K+) ion channels where "hydrophobic gating" is observed, an "on/off" behavior where the channels opens and closes for ion flow due to changes in the degree of pore wetting and presence of nanobubbles. 52–54 In biological ion channels, the current depends on the degree to which the ion channels are wet with liquid which, in turn, was found to depend on pore diameter, on the hydrophobic nature of atoms lining the pore and the applied voltage. 52 In our case, the 2D materials are largely hydrophobic, and wetting of the surface is a challenge. We explored an alcohol (ethanol) pre-wetting procedure in the context of sub-nm pores to maximize the amount of electrolyte that flows through the pore and to maximize the measured current.

The hydrophobic nature of 2D material solid-state nanopores has been previously observed and ethanol-prewetting of MoS_2^5 and WS_2^{45} was found to help obtain measurable ion currents

consistent with the pore size. Wetting can be probed further by applying external pressure to force the liquid transport through the pore.⁵⁵ The general concepts of wetting and de-wetting of pores used here are not new. Difficulty of pore wetting, the "dry", "wet" and "partially-wet" states of hydrophobic solid-state (silicon nitride) and polymer pores with diameters of the order of ~ 10 nm and ~ 100 nm, and the corresponding hysteretic behavior observed in *I-V* curves, have been reported a while ago.^{18,19,54} A hydrophobic pore can transition between the dry (non-conducting) and the wet (conducting) state upon voltage application. As voltage is increased, the pore can transition to a conducting state at higher bias resulting in an apparent non-linear *I-V* curve. This phenomenon was referred to as "voltage-induced gating"¹⁹ and "electric-field-induced wetting and dewetting"¹⁸ of a fabricated hydrophobic pore. Therefore, by applying voltage, a hydrophobic pore can be forced into a partially or fully-wet, conducting state. In this fully conducting state, the pore allows a maximum current possible based on its size, *i.e.*, the same current as in a hydrophilic pore of the same size. In addition, MD simulations have shown ionic "memcapacitive effects" and hysteresis loops (*I-V* measurement in a loop with no crossover) in nanopore systems, that depend on frequency and were proposed to arise from polarizability of ionic solutions.⁵⁶

Non-linearities in *I-V* curves can originate from hydrophobic effects and also from the ion confinement effects in small diameter pores, when their sizes are comparable to sizes of hydrated ions and Debye lengths. In biology, hydrophobicity is an essential property for ion channel behavior and gating, and it can be an inherent property of the pore. For example, stable gas pockets ("bubbles") can form inside hydrophobic regions of the pore; a sub-nm-wide pore region is required to make the bubbles stable long enough to observe relevant biological effects and when bubbles break, ions and water molecules flow through.⁵⁴ Analogous effects could be expected in solid-state pores and, because they are fabricated, these pores could serve as model systems to study such effects further and design artificial pores with specific functions. For example, according to modeling of MoS₂ pores, water flux can vary depending on whether Mo only, S only or mixed atoms, Mo and S, are at the edges.¹ Another approach to controlling the degree of hydrophobicity would be to coat the 2D pores, for example by atomic-layer-deposition of TiO₂, as demonstrated on graphene pores, to make them hydrophilic while only slightly increasing the pore thickness.³⁰ It is interesting to note that the non-linearity in *I-V* measurements is largely absent in molecular dynamics simulations⁴ and this is yet to be understood.

Pores may be dynamic in shape and change their conformations and edge termination – like in ion channels, this is a possibility for solid-state pores as well, but it is hard to probe directly

and more thermodynamic modeling would be beneficial to inform the experiment. It is likely that the pore structure could change over time. Atomic-scale fluctuations at the pore edge could have additional contributions to the degree of hydrophobicity inside of the atomic-scale pores. In biological pores, nanobubbles within the pore have been theoretically considered as possibly responsible for ion channel gating.⁵⁴ The extent to which the different parts of the pore itself are hydrophilic or hydrophobic depends on the ion channel diameter, the applied voltage and the local properties of pore edges and their interactions with ions and water molecules.⁵² Future studies can attempt to directly probe effects of these parameters in atomic 2D pores and the degree to which these effects can be controlled at the atomic scale.

Noise characteristics of single atomic pore chips. In addition to I-V characteristics, we find that the power spectral density (PSD) of these states yields insights into frequency-dependent properties and can be used to help determine the extent to which a zero-D pore is wet. PSD in solid-state nanopores is given as:

$$PSD = \frac{I^2 A}{f^{\alpha}} \quad (Eq. 1)$$

where I denotes the ionic current, A is the noise coefficient, α is the low frequency noise component and f is the frequency.⁵⁷ The PSD acquired at different stages of the wetting process for Pore 4 are shown in **Figure 4(d)**. For the bare electrodes (black), we obtain a noise coefficient of $A = 2 \times 10^{-7}$ and noise component of $\alpha = -0.3$, which is representative of instrumentation noise. Additionally, the spectrum for bare electrodes is identical to the PSD for a de-wet, incompletely wet pore (red), suggesting the absence of a conducting ion channel. For Pore 4 (2 Mo, 7 S) completely wet with ethanol (navy blue), we note $A = 5 \times 10^{-6}$ and $\alpha = -0.47$, which is similar to that of the pristine MoS₂ membrane wet with ethanol (green, $A = 7 \times 10^{-5}$, $\alpha = -0.14$). Crucially, the PSD for both cases exhibits a decrease in the sub-10² Hz regime (**Figure 4(c)**) compared to the rest of the frequency range, and is characteristic of 1/f noise in conducting solid-state pores.^{4,45,58,59} This is in stark contrast to the flat PSD obtained for both bare electrodes and de-wet pore, and suggests that ethanol is essential in creating a conducting ion channel through either intrinsic defects (in the pristine membrane) or STEM-fabricated zero-D pores (in Pore 4). A combination of I-V and noise analysis can therefore be utilized to better understand these states (States 1, 2, and 3) to determine whether a sub-nm pore is completely wet.

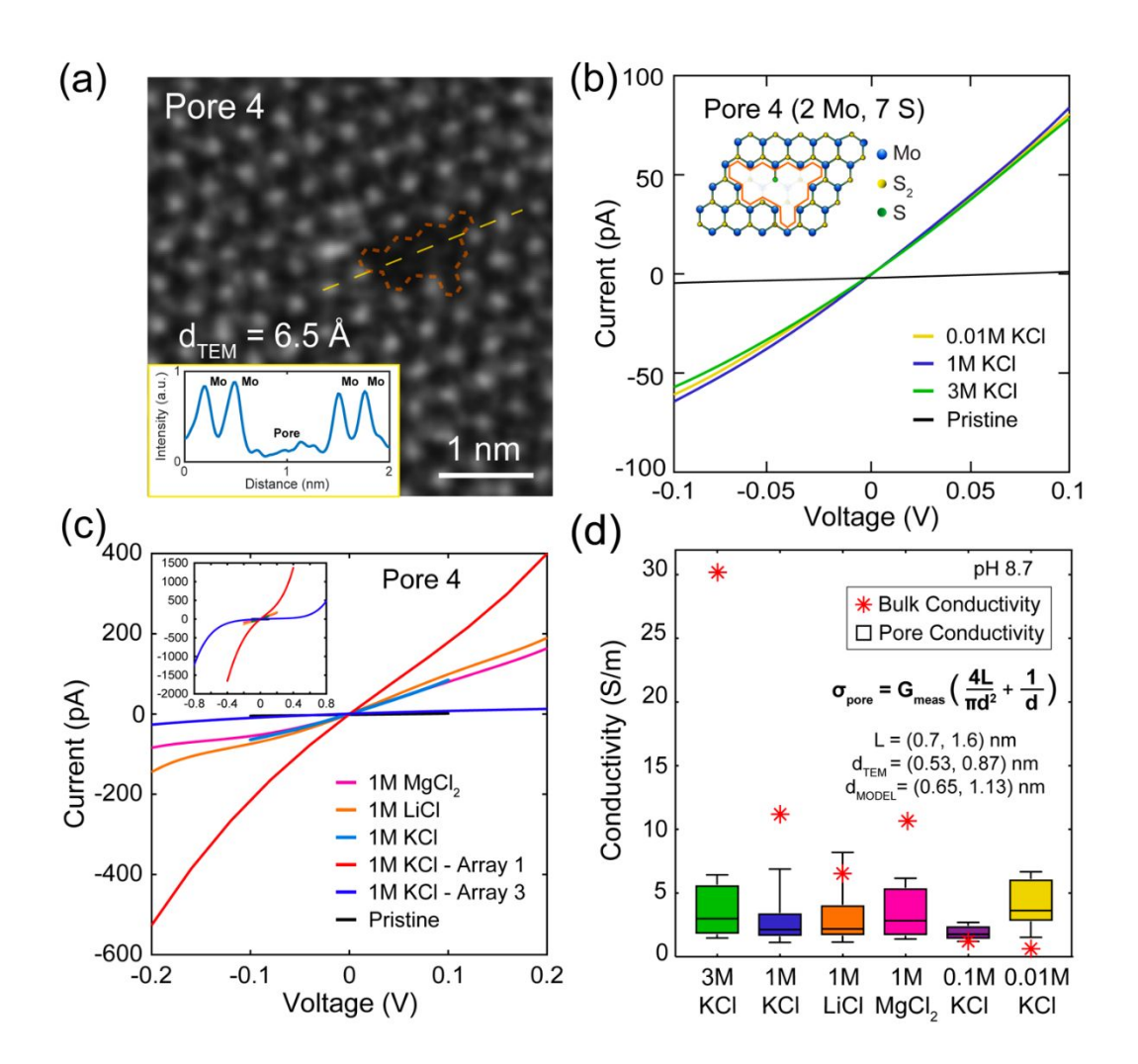


Figure 5. Ion current-voltage curves and pore conductivities calculated from a bulk model.

(a) AC-STEM image and (inset) intensity profile of a sub-nm pore (Pore 5) with $d_{TEM} = 0.65$ nm, where $d_{TEM} = \sqrt{{}^{4A_{TEM}/\pi}}$ and A_{TEM} is the pore area. (b) I-V characteristics and (inset) schematic of Pore 5 for various molarities of KCl – 10 mM (yellow), 1 M (navy), and 3 M (green). (c) I-V curves for Pore 5 obtained with different salt solutions – 1 M LiCl (orange), 1 M MgCl₂ (pink), 1 M KCl (light blue) – and a pristine MoS₂ membrane (black). Also shown in (c) are the current-voltage curves for arrays of sub-nm pores (labelled as Array 1 and Array 3) produced with low (dose 1, red) and high (dose 3, blue) doses of focused ion beam irradiation reproduced here from previous work for comparison⁴. (d) Pore conductivities of chloride-based salts (pH 8.7) including 1 M LiCl (orange), 1 M MgCl₂ (pink) and KCl at concentrations of 3 M KCl (green), 1 M KCl (navy), 0.1 M KCl (purple) and 0.01 M (yellow) from 3 different sub-nm MoS₂ pores (Pores 2-4) are presented. Each bar includes pore conductivity derived from Equation 2 (shown in inset) for upper and lower bounds of thickness (L = 0.7 nm, 1.6 nm) and diameter ($d_{TEM} = 0.53$ nm, 0.87

nm, and $d_{Model} = 0.65$ nm, 1.13 nm). Bulk conductivities of these salt solutions are plotted for comparison as asterixis (red).

Another example of such a zigzag-armchair pore, Pore 4, is shown in **Figure 5**. A HAADF image of this pore is shown in **Figure 5(a)**, alongside its atomic edge configuration shown in the inset of **Figure 5(b)**. Pore 4 has 2 Mo atoms and 7 pairs of S atoms missing, shown as (xii) in **Table 1**, corresponding to a geometric area of $0.94 \, \mathrm{nm^2}$. This is, again, confirmed by the Z contrast produced across the pore (yellow line) in the inset of **Figure 5(a)**. In the case of Pore 5 (which is our third I-V scenario), abiding by the procedure outlined in **Figure 3(a)** (i)- (iv), we obtain the current-voltage measurements for multiple salt solutions and salt concentrations. First, we examine the conductance in the case of different salt concentrations in **Figure 5(b)** – 10 mM KCl (yellow), 1 M KCl (blue) and 3 M KCl (green) at pH 8.7. We clearly observe a phenomenon where the zero-D pore demonstrates an ionic conductance largely independent of the salt concentration, all three *I-V* of 10 mM, 1 M and 3 M KCl correspond to $G \sim 0.71 \, \mathrm{nS}$, $0.69 \, \mathrm{nS}$ and $0.75 \, \mathrm{nS}$, respectively, extracted as slopes of the linear fits to the *I-V* curves in the voltage range $\pm 100 \, \mathrm{mV}$.

I-V characteristics acquired for other salt solutions such as 1 M LiCl (orange) and 1 M MgCl₂ (pink) from an applied voltage range of \pm 200 mV are presented in **Figure 5(c)**. Given that these salt solutions have a significant difference in bulk conductivity (precisely, 1 M LiCl = 9.5 S/m, 1 M MgCl₂ = 12.3 S/m, 10 mM KCl = 0.14 S/m, 1 M KCl = 10.8 S/m and 3 M KCl = 29.28 S/m), it is noteworthy that we observe a small change in pore conductance value in these salt solutions through the zero-D pore in the ± 200 mV range, compared to the difference in respective bulk values. In contrast to the typical linear behavior of nm-sized pores, these zero-D pores also exhibit somewhat non-linear current-voltage curves. These non-linearities are more evident at higher voltages, as shown in the inset of Figure 5(c), which are I-V curves obtained from an array of sub-nm zero-D pores produced in the MoS₂ membrane by FIB irradiation and measured over a range of \pm 800 mV.⁴ These arrays contained on average \sim 300 - 1200 small pores of diameters smaller than ~ 1 nm (out of which ~ 30 - 240 pores on average were larger than 0.6 nm – the hydrated K+ ion diameter) and these samples exhibited G in a wide range ~ 0.5 nS to 50 nS in 1M KCl (these G values are for the dose used for "Array 3"). While the particular sample "Array 3" in Figure 5(c) is found to be less conducting than Pore 4, the mean conductance of all such measured samples, FIB irradiated at the same dose, was larger than G of Pore 4, with a mean conductance value of ~ 20 nS.⁴ Additional, slight non-linearity is also observed in case of multiple

Supplementary Figure S2 a bar graph of calculated conductance ranges by fitting a line to I-V curves over several voltage ranges, such as \pm 30 mV, \pm 50 mV, \pm 100 mV, \pm 200 mV from zero-D pores measured in this work (Pores 2, 3, 4) in **Supplementary Figure S2.** We note that there is a difference of \pm 0.01 to 0.086 nS across different voltage range for a given zero-D pore, reflecting the degree of non-linearity. About 42% of the zero-D pores fabricated, yielded a conductance of 0.7 nS- 0.9 nS across various cation-based chloride salt solutions from 0.1 M to 3 M with a slight variation in conductance (\pm 0.1 nS). While the other devices showed hysteretic I-V, the current was immeasurably small and/or pores could not be wet.

Calculation of pore conductivities based on measured conductance and pore sizes. We can estimate pore conductivities based on measured conductance G and effective pore diameters from TEM images prior to I-V measurements, d_{TEM} , and those obtained from pore models, d_{Model} , assuming a known pore thickness, L, discussed below. Using a continuum model applicable for bulk behavior in nm-size and larger diameter solid-state pores, conductance G can be well-described for solid-state pores⁶⁰:

$$G = \sigma \left(\frac{4L}{\pi d^2} + \frac{1}{d}\right)^{-1} \qquad (Eq. 2)$$

where σ is conductance of the solution that depends on the molarity, d is effective pore diameter (assuming circular pores) and L is the effective pore thickness; d and L correspond to the effective dimensions of the ionic conducting cylindrical channel. As d and L approach zero, ions are confined in spaces of dimensions comparable to ionic radii, and the ion concentrations, mobilities and hydration are theoretically different from bulk^{12,26,49} Perez *et al.*²⁷ recently proposed an analytical expression similar to $Eq.\ 2$, based on inputs from molecular dynamics simulations, for small MoS₂ pores, but with a modified multiplication pre-factor σ in $Eq.\ 2$, to reflect the reduced K⁺ and Cl⁻ ion concentrations and mobilities compared to bulk (See the Equation in SI section 5). In other words, for small pores, the authors proposed that one can consider that a small pore has a modified conductivity compared to bulk, and $Eq.\ 2$ can be modified by replacing σ with another function of diameter, $\sigma_{pore}(d) \neq \sigma_{bulk}$. For an effective MoS₂ pore diameter around 1 nm, the ion mobility was computed to be about 60% of bulk mobility and ion concentration to be about 30% of bulk concentration.²⁷

In Equation 2, the total resistance $R=1/G=R_{pore}+R_{access}$, where $R_{pore}=(\frac{4L}{\sigma\,\pi d^2})$ is the resistance of the pore, which is modeled as a cylinder. The second term, $R_{access}=(\frac{1}{\sigma d})$ is the so-called "access" resistance, arising from the solution in the top and bottom hemispheres on the two sides of the membrane. In our case, the effective pore diameter, d, and the effective pore length, L, are comparable (both ~ 1 nm). For L in our calculations and for error estimation, we use here a range of values for L previously used, from L=0.7 nm 4,13 (the geometric thickness of the MoS₂ membrane) up to L=1.6 nm estimated from previous MoS₂ pore conductance measurements on larger diameter pores. For the effective diameter estimates here, we use, $A_{TEM}\sim 0.22$ nm² to 0.59 nm², and $A_{Model}\sim 0.34$ nm² to 1.0 nm², yielding d_{TEM} from ~ 0.53 nm to ~ 0.87 nm, and d_{Model} from 0.65 to 1.12 nm. The pores could be thicker if there is contamination and have larger diameters if they expanded over time.

From measured conductances, G_{meas} , we can estimate the equivalent pore conductivities that would yield these conductances, a perspective proposed by Perez *et al.* to view sub-5 nm diameter MoS_2 pores,²⁷ as

$$\sigma_{pore} = G_{meas} \left(\frac{4L}{\pi d^2} + \frac{1}{d} \right), \qquad (Eq. 3)$$

,where G_{meas} is the measured conductance, d is the diameter, and L is the pore thickness. Using measured conductance from zero-D pores, a range of pore diameters from AC-STEM images, from corresponding pore models and L values from 0.7 nm -1.6 nm^{5,25}, we calculated σ_{pore} , plotted for various salt solutions and concentrations in **Figure 5(d)**. Therefore, error bars in **Figure 5(d)** reflect uncertainties in *d* from our analysis. Errors are plotted using the ranges of d_{TEM} and d_{MODEL} for d, and the range from 0.6 nm to 1.6 nm for *L*.

For comparison, also plotted in red symbols are the corresponding bulk conductivities for each solution. Our results at 1 M KCl display $\sigma_{pore}/\sigma_{bulk} = 25\%$ - 65% (for 0.53 nm - 0.87 nm diameter pores) which also somewhat agrees with the trend from molecular dynamics simulations for sub-5 nm MoS₂ pores where they reported 8% - 40% (for 0.7 nm - 1.25 nm diameter pores).²⁷

The conductance values observed are a bit smaller than 1 nS and similar across different concentrations and cations (K⁺, Li⁺, Mg⁺⁺). Furthermore, I-V characteristics are non-linear, although non-linearities are mostly pronounced for higher voltages (**Figure 5(c)**). While hydrophobicity can lead to such observations as discussed above, another contributing factor in

small pores is the spatial confinement and interactions experienced by the salt ions when the pore is of the similar size to the size of the hydrated salt ions. This has also been shown in other MD simulations where dehydration of the first hydration layer, orientation of water dipoles inside and outside the pore dictate the type of non-linearities observed in these small measurable currents.³ Further, Richards *et al.*¹⁷ showed that ion transport is hindered when pore size is comparable to dimensions of hydrated ion molecules and that partial dehydration is the main factor for energy barriers.^{17,64} Ion selectivity of pores is another aspect that has been experimentally investigated, such as in cation-selective sub-nm graphene pores¹⁰ but the available body of reproduced experimental work is limited.¹²

Saturation of conductance vs. molarity. We observe a saturation in conductance across 3 M to 0.01 M KCl and other salt solutions. For larger, nanometer size solid-state pores, this saturation in KCl solution was previously observed to occur for molarities below ~ 0.1 M 22,65 . This molarity corresponds to Debye length, $\lambda_D \approx 1$ nm for 0.1 M KCl, equivalent to about four water molecule diameters, and $\lambda_D \approx 3$ nm for 10 mM KCl. We see that for a zero-D pore (d < 1 nm), the saturation of G with decreasing molarity, M, occurs at higher molarities than for one-order-of-magnitude larger, nm-size pores. This is likely because the characteristic pore size d is now comparable to λ_D even at relatively higher molarities such as 1 M – 3 M KCl, where $\lambda_D \approx 0.1$ - 0.3 nm, explaining why we observe similar conductances for 3 M and 10 mM KCl.

At low molarity < 0.1 M KCl, we observe in **Figure 5(d)** that conductance is similar or larger than expected from the corresponding bulk value and assuming an idealized inert transport channel governed by Eq. 2.66 This is because Equation 2 does not take directly into account that pores have charged surfaces (although this is effectively taken into account in Eq. 3 by assuming some equivalent pore conductivity, σ_{pore}). For "large" pores, the pore's surface charge effect on G can be negligible given that surface charges are screened within Debye's length $\lambda_D \approx 0.3$ nm in 1 M KCl. It was previously established that as the system size decreases approximately below micron and nm-scales, surface charge effects on G can be noticeable on ionic transport at molarities below ~ 0.1 M, and transport can even become fully governed by surface charges in nanofluidic channels in very "small" systems and/or very "low" molarities. ⁶⁶ The lower the molarity, the larger the size of the channel for which surface charge effects on G are noticeable.

In nanofluidic channels, as molarity M decreases, conductance transitions from a regime where $G \sim M$ to the regime where G saturates as a function of M at low molarities.⁶⁶ This

dependence was established experimentally in silicon nitride (see for example SI in Ref. 64)⁶⁵ and 2D pores, with negative surface charge densities of the order \sim - 0.01 C/m² to - 0.1 C/m² reported²² for MoS₂ pores with diameters d > 2 nm by fitting G vs. M and dependent on pH. This "low-molarity transport behavior", where the definition of what is "low" depends on the system size, is explained by electrostatic effects of the channel's surface charge on the fluid. The smaller the system, the higher the molarity at which this saturation occurs: a charged pore surface attracts oppositely charged counterions from solution while repelling co-ions. This results in a charged layer forming close to the pore walls, called the double layer, and this layer screens the immobile surface-charge. To maintain charge neutrality the number of mobile counterions in a channel can exceed the bulk ion concentration and dominate transport.⁶⁶

Low conductance presents a challenge for higher bandwidth measurements, requiring capacitance minimization to reduce noise and current contributions from capacitor charging. Compared to zero-D MoS₂ pores supported on Si chips (**Figure 1**), pores fabricated on low-capacitance glass chips ^{67,68} exhibited a lower noise but significantly higher polymer contamination (see **Supplementary Figures S4 and S5**). Future studies will benefit by using low-capacitance platforms combined with low-noise transimpedance amplifiers^{69–72} to get insight into the short timescale behavior of both ion channels and zero-D solid state pores, such as to resolve short current events and probe the mechanisms of the channel on/off dynamics.⁷¹

Conclusions and future directions

With the help of the state-of-art transmission electron microscopy and advancement of 2D material devices, we report an elaborate device fabrication of a single zigzag-armchair zero-D pores which have definite pore edges and known atomic composition of pore edges. In this regime of sub-nm pores, we observe the conductance of zero-D pore is largely independent of bulk conductivity and dependent on the applied bias to drive ions through the pores. We observe a quenched ionic conductance (~ 0.8 nS) compared to nm-scale pores in case of pores with the diameters similar to the size of hydrated salt ions, and the conductance saturation vs. molarity in a wide ion concentration range. This conductance is close to values recently reported in other solid-state atomic-scale systems where ion transport was confined to ~ 1 nm in one or more dimensions, such as in single 0.8 nm and 1.5 nm diameter, 10-nm-long carbon nanotubes.^{6,7,12}

Blockade of ion passage by small pores and dehydration of solvated ions were hypothesized as mechanisms to explain experimentally observed suppressed ionic current at low voltages and non-linear I-V curves as voltage is increased.^{2,5} We are now able to fabricate Zero-D pores that mimic the bio pores, with good reproducibility and similar ionic conductance (~ 0.6 - 1 nS) to that of proteins that occur naturally.^{70,71} Another important aspect of these biological pores is their transport mechanisms and selectivity for specific cations or anions. This feature is yet to be studied in our zero-D, future experiments can investigate conductance at various pH and attempt to modify the surface charge of these zero-D pores. We were not able to image the nanopores after the ionic conductance measurements. Future studies can also attempt AC-TEM imaging of the pores after the ionic measurements and examine the extent to which these measurements result in some geometry changes of the pore.

Several limitations existed in our study. TEM images correspond to pores before ionic measurements and we were not able to image the pores after the ionic measurements. Also, because the membrane is contaminated after being in salt solution, the baseline ionic current was established from pristine membrane samples (with no intentional pores) that are not the same samples used for pore TEM drilling, although all samples came from the nominally identical batch of membranes (from the same CVD growth) and same fabrication procedures.

Pretreatment with ethanol here is seen to enhance the pore hydrophilicity and enable measurements of small but measurable currents through the pore. Studies have proven that the methanol or ethanol/water solvent mixture change the dielectric constant of the solution which could alter the surface charge on the pore in a favorable way to allow ions to translocate.⁷³ This wetting technique aided by an alcohol is being used by several experimental studies already on 2D nanopores and nanochannels.^{5,8,25,30,45} So far, our experimental investigation leads to the conclusion that wetting the pore is possible through a polar solvent such as ethanol which is important for translocating ions through the entirety of the zigzag-armchair pore. Future studies may design pore edges to further control ion translocation through the pores, maybe also guided by molecular dynamics simulation studies addressing pore stability and transport.

Methods

CVD Growth: Monolayer MoS_2 flakes were grown using CVD processes reported in previous works.³¹ Solutions of 0.2% sodium cholate growth promoter and 18×10^{-3} m ammonium heptamolybdate were spun onto piranha-cleaned Si substrates coated with 300 (150) nm of SiO₂, which were then loaded into the center of a 1 in. tube furnace (Thermo Scientific Lindberg/Blue

M). For the MoS_2 growth, samples were heated under N_2 gas flow (700 sccm) at a rate of 70 °C min⁻¹ and held at 750 °C for 15 min. Approximately 100 mg of sulfur precursor placed 22 cm from the substrates was kept at 180 °C during the growth procedures. Samples were rapidly cooled to room temperature by opening the furnace.

Device Fabrication: MoS₂ crystals were transferred from Si/SiO₂ substrates with a focused ion beam (FIB) hole (~ 150 – 200 nm in diameter) using a wet etch technique. Crystals were first coated with C4 PMMA while aqueous 1 M KOH solution was used to etch away the underlying substrate. After being washed in deionized (DI) H₂O, crystals were scooped onto TEM grids and dried for 30 min. Polymer liftoff and sample cleaning were performed using acetone and rapid thermal annealing in Ar: H₂ gas at 300 °C, respectively. While tears and other failures modes of membranes and pores are possible, we have optimized our procedure to have continuous triangular flakes of MoS₂, that are sealed to the supporting chip by annealing. When there are tears, the measured current is significantly larger; for example, for pores larger than 1 nm in diameter, the current is in the tens of nA's and for larger tears significantly more. We had a few samples that clearly broke as evidenced by a sudden surge of current, followed by confirmation in microscopy. The small magnitude of current is an indicator of two possible outcomes: either the conducting pore is small or that the membrane and/or pore are not fully wetting to allow maximum current flow based on pore size.

Pore Fabrication and Imaging: Sub-nm MoS_2 pores were fabricated and imaged using a Cs-corrected JEOL ARM 200CF STEM operating at 80 kV. The spherical aberration coefficients was generally $Cs \sim 100$ nm. Pores were drilled by switching the instrument with a 22 pA probe current to selected area (1×1 nm) exposure and monitoring the radiolysis process. After approximately 10 seconds, the instrument was switched back to full scan (13 × 13 nm). Images were obtained using a HAADF detector with a collection angle of 54–220 mrad and 10 cm camera length. Only one image was acquired after pore drilling to minimize beam-induced knock-on damage.

We note that TEM images provide structural information *only* for the initial, as-fabricated pores in vacuum, prior to any I-V measurements. This presents a limitation here as well as previous nanopore studies where it was experimentally challenging to locate and image the pores after ionic measurements. Previous similar individual pore studies have not measured the pore diameter directly.^{2,5} It is possible and likely that once the pores are taken out of vacuum and immersed in

solution their structure can change and these changes can include pore clogging as well as pore etching over time in salt solution². Moreover, these changes could be amplified by the applied electric field to enlarge the pores.¹³ Here, we limit the applied voltage to 0.1 V and we also calibrate our conductance values using results from larger 2D pores ^{4,25,34} as expected upper bounds for our sub-nm pores (~ 1 nS to 10 nS). Conductance larger than 1 nS may strongly indicate that the pores have expanded beyond 1 nm in diameter over the course of handling and measurements.

There can be several complications in device fabrication. While we did not probe the extent of debris, we observe that annealing is critical to seal the membrane and make it not leaky or lift off in ionic solution. We go by the amount of measured ionic current as an indicator of the degree of holes or current paths. We did not observe membranes lifting off, but we observed pore expansions and increase in ionic current if higher voltages are applied.

Pore Diameter Determination: The geometric models (**Table 1** and pore schematic in figures) were carefully created based on the missing atoms observed in TEM images and the 3D view such as in **Figure 2f**. These models do not consider the electron cloud space or the orbital distance which can perhaps be accounted for through Molecular Dynamics (not employed here). Additionally, we assume that the pore edges follow a perfect lattice from which the missing atoms are simply cut out. In the real TEM images however, we see that there can be lattice distortions and bunching of Mo atoms, such that the distances between atoms along the edge can vary and be slightly shorter or longer than in the pristine lattice. Furthermore, in the real pores there is a consistent uncertainly in the number of S atoms specially along the pore edges due the weaker intensity of S atoms produced in contrast to heavier Mo atoms. Therefore, we use both the pore areas obtained through TEM images (d_{TEM}) (see **Figure S1**) and geometric models (d_{MODEL}).

Definition of effective pore diameters used in this study: For the purpose of careful analysis we define two pore diameters, d_{TEM} and d_{Model} , both calculated as diameters of equivalent circles with the same area as the pore, where the pore area is estimated in two different ways. For $d_{TEM} = \sqrt{\frac{4A_{TEM}}{\pi}}$, we estimate the pore area, A_{TEM} , directly from the AC-TEM zoomed in image of the pore and the scale bar is obtained experimentally in the TEM. This image analysis is done using functions and filter in software ImageJ (See Image Processing SI S1). For $d_{Model} = \sqrt{\frac{4A_{Model}}{\pi}}$, we use the area calculated from the geometric model of the pore and the scale bar is obtained theoretically from the atomic distances in the 2D MoS₂ lattice. An example analysis and

calculation of d_{TEM} for *Pores 2,3,4*, are given in Figure SI S1. The differences in values of d_{TEM} and d_{Model} primarily come from the deviation of the pore edges from the perfect lattice, for example if a pore has atoms that are bunched up on the edges, such as in **Figure 1f**.

Ionic Measurements: EPC-10 HEKA amplifier setup⁷⁴ with Ag/AgCl electrodes was used to perform ionic measurements on our devices. 1 M KCl and other salt solutions (with 10 mM EDTA and 1 mM Tris; measured solution conductivity = 11.18 S/m for 1 M KCl, pH 8.7) solution was prepared using DI water, and the conductivity and pH were measured with Accumet XL-20 pH conductivity meter. Similar measurements were also conducted for glass chips 67,68 but on the Chimera amplifier setup with higher-bandwidth (1-MHz).⁷⁵ Prior to ionic measurements, the device was annealed at 300 °C in an Ar : H₂ environment for 90 minutes. The device was then immersed in a 50% water-ethanol solution typically for 15 to 30 minutes, which we empirically found to help wetting and formation of ionic channels through the pores. Some samples were immersed for longer time from 3-5 hours to 12 hours. The device in ethanol was intermittently bubbled in the solution with the glass pipette to ensure no air bubbles are left trapped in the device. Voltage (V) was applied across the pore while measuring the ionic current (I). Voltage bias was kept below ± 0.1 V for most pores in this work. A custom-built LabView Software is used to run experiment on Heka amplifier, I-V sweeps and time-trace features of this program was utilized.⁷⁴ Majority of the I-V measurement involved a sweep rate of 5 mV per second, 10 mV per second was used for faster acquisition. All I-V sweeps were offset to start at zero and were averaged in case of multiple I-V sweeps. "Pristine membranes" (membranes without holes) are control devices and not the same devices used to drill pores. It was challenging for us to measure in salt solution and then use the same membrane again to drill the pore and remeasure in solution. This is because the membrane gets dirty from the salt solution and there are additional possible failure modes such as membrane breaking. Therefore, we rely on control samples (membranes without drilling) to establish the baseline current, and on samples with drilling to establish the current through the pore. Because these are not the same samples, this presents a limitation of the present study.

Associated Content

Supporting Information. The supplementary information includes: Conductance of zero-D pores, Samples containing multiple (2-3) sub-nm MoS₂ pores, Current-voltage and noise characteristics of sub-nm MoS₂ pores on low-capacitance glass chips, Image processing to determine the TEM

pore area and diameter, Molecular dynamics (MD) simulation-based analytical equation²⁷ for sub-5 nm-diameter MoS₂ pore conductance in 1 M KCl.

Author Information

Corresponding Author. *Email: drndic@physics.upenn.edu

Author Contributions. J.P.T, P.M.D and M.D conceived the project idea. J.P.T and P.M.D grew 2D materials, fabricated devices, and performed image analysis. J.P.T performed ionic measurements and data analysis. P.M.D conducted the AC-TEM work. The manuscript was written through contributions of all authors. All authors have given approval to the final version of the manuscript.

Notes. The authors declare no competing financial interest.

Acknowledgements

AC-STEM imaging and nanopore drilling were executed at the Center for Advanced Materials and Nanotechnology at Lehigh University with assistance from Dr. Robert Keyse. We thank Prof. Adrien Nicolai, Prof. Patrick Senet and Dr. Daniela Barrios from the University of Bourgogne for discussions of the implications of their molecular dynamics models²⁷ for this work, Dr. Sanjin Marion and Prof. Aleksandra Radenovic from EPFL for useful discussions of MoS₂ pore measurements and pore wetting aspects. This work was supported by the NSF through the University of Pennsylvania Materials Research Science and Engineering Center (MRSEC) DMR-1720530 as well as NSF Grants EFRI 2-DARE 1542707, NSF DMR 1905045 and NSF EAGER 1838456, and NIH R21 HG010536. This work was performed in part at the University of Pennsylvania's Singh Center for Nanotechnology, an NNCI member supported by NSF Grant ECCS-1542153. J.P.T. acknowledges fellowship support from the Vagelos Institute of Energy Science and Technology.

References

- (1) Heiranian, M.; Farimani, A. B.; Aluru, N. R. Water Desalination with a Single-Layer MoS 2 Nanopore. *Nature Communications* **2015**, *6*, 1–6. https://doi.org/10.1038/ncomms9616.
- (2) Jain, T.; Rasera, B. C.; Guerrero, R. J. S.; Boutilier, M. S. H.; O'Hern, S. C.; Idrobo, J.-C.; Karnik, R. Heterogeneous Sub-Continuum Ionic Transport in Statistically Isolated Graphene Nanopores. *Nature Nanotechnology* **2015**, *10* (12), 1053–1057. https://doi.org/10.1038/nnano.2015.222.

- (3) Sahu, S.; Di Ventra, M.; Zwolak, M. Dehydration as a Universal Mechanism for Ion Selectivity in Graphene and Other Atomically Thin Pores. *Nano Letters*. 2017, pp 4719–4724. https://doi.org/10.1021/acs.nanolett.7b01399.
- (4) Thiruraman, J. P.; Fujisawa, K.; Danda, G.; Masih Das, P.; Zhang, T.; Bolotsky, A.; Perea-López, N.; Nicolaï, A.; Senet, P.; Terrones, M.; Drndić, M. Angstrom-Size Defect Creation and Ionic Transport through Pores in Single-Layer MoS2. *Nano Letters* **2018**, *18* (3), 1651–1659. https://doi.org/10.1021/acs.nanolett.7b04526.
- (5) Feng, J.; Liu, K.; Graf, M.; Dumcenco, D.; Kis, A.; Di Ventra, M.; Radenovic, A. Observation of Ionic Coulomb Blockade in Nanopores. *Nature Mater* 2016, 15 (8), 850–855. https://doi.org/10.1038/nmat4607.
- (6) Yao, Y.; Taqieddin, A.; Alibakhshi, M. A.; Wanunu, M.; Aluru, N. R.; Noy, A.; Taqieddin, A.; Alibakhshi, M. A.; Wanunu, M.; Aluru, N. R.; Noy, A. Strong Electroosmotic Coupling Dominates Ion Conductance of 1.5 Nm Diameter Carbon Nanotube Porins. *ACS Nano* **2019**, *13*, 12851–12859. https://doi.org/10.1021/acsnano.9b05118.
- (7) Tunuguntla, R. H.; Henley, R. Y.; Yao, Y.; Pham, T. A.; Wanunu, M.; Noy, A. Enhanced Water Permeability and Tunable Ion Selectivity in Subnanometer Carbon Nanotube Porins. *Science (New York, N.Y.)* **2017**, *357*, 792–796.
- (8) Esfandiar, A.; Radha, B.; Wang, F. C.; Yang, Q.; Hu, S.; Garaj, S.; Nair, R. R.; Geim, A. K.; Gopinadhan, K. Size Effect in Ion Transport through Angstrom-Scale Slits. *Science* **2017**, *358* (6362), 511–513. https://doi.org/10.1126/science.aan5275.
- (9) Gopinadhan, K.; Hu, S.; Esfandiar, A.; Lozada-Hidalgo, M.; Wang, F. C.; Yang, Q.; Tyurnina, A. V.; Keerthi, A.; Radha, B.; Geim, A. K. Complete Steric Exclusion of Ions and Proton Transport through Confined Monolayer Water. *Science* 2019, 363 (6423), 145–148. https://doi.org/10.1126/science.aau6771.
- (10) O'Hern, S. C.; Boutilier, M. S. H.; Idrobo, J. C.; Song, Y.; Kong, J.; Laoui, T.; Atieh, M.; Karnik, R. Selective Ionic Transport through Tunable Subnanometer Pores in Single-Layer Graphene Membranes. *Nano Letters* **2014**, *14* (3), 1234–1241. https://doi.org/10.1021/nl404118f.
- (11) Rollings, R. C.; Kuan, A. T.; Golovchenko, J. A. Ion Selectivity of Graphene Nanopores. *Nat Commun* **2016**, 7 (1), 11408. https://doi.org/10.1038/ncomms11408.
- (12) Thiruraman, J. P.; Masih Das, P.; Drndic, M. Ions and Water Dancing through Atom-Scale Holes: A Perspective toward "Size Zero". *ACS Nano* **2020**, *14* (4). https://doi.org/10.1021/acsnano.0c01625.
- (13) Feng, J.; Liu, K.; Graf, M.; Lihter, M.; Bulushev, R. D.; Dumcenco, D.; Alexander, D. T. L.; Krasnozhon, D.; Vuletic, T.; Kis, A.; Radenovic, A. Electrochemical Reaction in Single Layer MoS ₂: Nanopores Opened Atom by Atom. *Nano Lett.* **2015**, *15* (5), 3431–3438. https://doi.org/10.1021/acs.nanolett.5b00768.
- (14) Krems, M.; Di Ventra, M. Ionic Coulomb Blockade in Nanopores. *J. Phys.: Condens. Matter* **2013**, *25* (6), 065101. https://doi.org/10.1088/0953-8984/25/6/065101.
- (15) Zwolak, M.; Wilson, J.; Di Ventra, M. Dehydration and Ionic Conductance Quantization in Nanopores. J. Phys.: Condens. Matter 2010, 22 (45), 454126. https://doi.org/10.1088/0953-8984/22/45/454126.
- (16) Zwolak, M.; Lagerqvist, J.; Di Ventra, M. Quantized Ionic Conductance in Nanopores. *Phys. Rev. Lett.* **2009**, *103* (12), 128102. https://doi.org/10.1103/PhysRevLett.103.128102.
- (17) Richards, L. A.; Schäfer, A. I.; Richards, B. S.; Corry, B. The Importance of Dehydration in Determining Ion Transport in Narrow Pores. *Small* **2012**, *8* (11), 1701–1709. https://doi.org/10.1002/smll.201102056.
- (18) Powell, M. R.; Cleary, L.; Davenport, M.; Shea, K. J.; Siwy, Z. S. Electric-Field-Induced Wetting and Dewetting in Single Hydrophobic Nanopores. *Nature Nanotech* **2011**, *6* (12), 798–802. https://doi.org/10.1038/nnano.2011.189.
- (19) Smirnov, S. N.; Vlassiouk, I. V.; Lavrik, N. V. Voltage-Gated Hydrophobic Nanopores. *ACS Nano* **2011**, *5* (9), 7453–7461. https://doi.org/10.1021/nn202392d.

- (20) Joshi, R. K.; Carbone, P.; Wang, F. C.; Kravets, V. G.; Su, Y.; Grigorieva, I. V; Wu, H. A.; Geim, A. K.; Nair, R. R. Precise and Ultrafast Molecular Sieving through Graphene Oxide Membranes. *Science (New York, N.Y.)* **2014**, *343* (6172), 752–754. https://doi.org/10.1126/science.1245711.
- (21) Surwade, S. P.; Smirnov, S. N.; Vlassiouk, I. V; Unocic, R. R.; Veith, G. M.; Dai, S.; Mahurin, S. M. Water Desalination Using Nanoporous Single-Layer Graphene. *Nature Nanotechnology* **2015**, *10* (5), 459–464. https://doi.org/10.1038/nnano.2015.37.
- (22) Feng, J.; Graf, M.; Liu, K.; Ovchinnikov, D.; Dumcenco, D.; Heiranian, M.; Nandigana, V.; Aluru, N. R.; Kis, A.; Radenovic, A. Single-Layer MoS2 Nanopores as Nanopower Generators. *Nature* **2016**, *536* (7615), 197–200. https://doi.org/10.1038/nature18593.
- (23) Marcus, Y. Ionic Radii in Aqueous Solutions. *Chem. Rev.* **1988**, *88* (8), 1475–1498. https://doi.org/10.1021/cr00090a003.
- (24) Tongraar, A.; Liedl, K. R.; Rode, B. M. Born–Oppenheimer Ab Initio QM/MM Dynamics Simulations of Na ⁺ and K ⁺ in Water: From Structure Making to Structure Breaking Effects. *J. Phys. Chem. A* **1998**, *102* (50), 10340–10347. https://doi.org/10.1021/jp982270y.
- (25) Liu, K.; Feng, J.; Kis, A.; Radenovic, A. Atomically Thin Molybdenum Disulfide Nanopores with High Sensitivity for DNA Translocation. *ACS Nano* **2014**, *8* (3), 2504–2511. https://doi.org/10.1021/nn406102h.
- (26) Graf, M.; Lihter, M.; Thakur, M.; Georgiou, V.; Topolancik, J.; Ilic, B. R.; Liu, K.; Feng, J.; Astier, Y.; Radenovic, A. Fabrication and Practical Applications of Molybdenum Disulfide Nanopores. *Nat Protoc* **2019**, *14* (4), 1130–1168. https://doi.org/10.1038/s41596-019-0131-0.
- (27) Pérez, M. D. B.; Nicolaï, A.; Delarue, P.; Meunier, V.; Drndić, M.; Senet, P. Improved Model of Ionic Transport in 2-D MoS ₂ Membranes with Sub-5 Nm Pores. *Appl. Phys. Lett.* **2019**, *114* (2), 023107. https://doi.org/10.1063/1.5061825.
- (28) Danda, G.; Drndi, M. ScienceDirect Two-Dimensional Nanopores and Nanoporous Membranes for Ion and Molecule Transport. **2019**, 124–133.
- (29) Schneider, G. F.; Kowalczyk, S. W.; Calado, V. E.; Pandraud, G.; Zandbergen, H. W.; Vandersypen, L. M. K.; Dekker, C. DNA Translocation through Graphene Nanopores. *Nano letters* **2010**, *10* (8), 3163–3167. https://doi.org/10.1021/nl102069z.
- (30) Merchant, C. A.; Healy, K.; Wanunu, M.; Ray, V.; Peterman, N.; Bartel, J.; Fischbein, M. D.; Venta, K.; Luo, Z.; Johnson, A. T. C.; Drndić, M. DNA Translocation through Graphene Nanopores. *Nano Letters* **2010**, *10* (8), 2915–2921. https://doi.org/10.1021/nl101046t.
- (31) Thiruraman, J. P.; Masih Das, P.; Drndic, M. Irradiation of Transition Metal Dichalcogenides Using a Focused Ion Beam: Controlled Single-Atom Defect Creation. *Adv. Func. Mats.* **2019**, *29* (52), 1904668. https://doi.org/10.1002/adfm.201904668.
- (32) Kuan, A. T.; Lu, B.; Xie, P.; Szalay, T.; Golovchenko, J. A. Electrical Pulse Fabrication of Graphene Nanopores in Electrolyte Solution. *Applied Physics Letters* **2015**, *106* (20). https://doi.org/10.1063/1.4921620.
- (33) Verschueren, D. V.; Yang, W.; Dekker, C. Lithography-Based Fabrication of Nanopore Arrays in Freestanding SiN and Graphene Membranes. *Nanotechnology* **2018**, *29*, 145302. https://doi.org/10.1088/1361-6528/aaabce.
- (34) Thakur, M.; Macha, M.; Chernev, A.; Graf, M.; Lihter, M.; Deen, J.; Tripathi, M.; Kis, A.; Radenovic, A. Wafer-Scale Fabrication of Nanopore Devices for Single-Molecule DNA Biosensing Using MoS2. *Small Methods n/a* (n/a), 2000072. https://doi.org/10.1002/smtd.202000072.
- (35) Ke, J.-A.; Garaj, S.; Gradecak, S. Nanopores in 2D MoS2: Defect-Mediated Formation and Density Modulation. *ACS Applied Materials & Interfaces* **2019**, *11*, 26228–26234. https://doi.org/10.1021/acsami.9b03531.
- (36) Liu, X.; Wood, J. D.; Chen, K. S.; Cho, E.; Hersam, M. C. In Situ Thermal Decomposition of Exfoliated Two-Dimensional Black Phosphorus. *Journal of Physical Chemistry Letters* **2015**, *6* (5), 773–778. https://doi.org/10.1021/acs.jpclett.5b00043.
- (37) Wang, L.; Boutilier, M. S. H.; Kidambi, P. R.; Jang, D.; Hadjiconstantinou, N. G.; Karnik, R. Fundamental Transport Mechanisms, Fabrication and Potential Applications of Nanoporous

- Atomically Thin Membranes. *Nature Nanotechnology* **2017**, *12* (6), 509–522. https://doi.org/10.1038/nnano.2017.72.
- (38) Jiang, Y.; Chen, Z.; Han, Y.; Deb, P.; Gao, H.; Xie, S.; Purohit, P.; Mark, W.; Park, J.; Gruner, S. M.; Elser, V.; Muller, D. A. Electron Ptychography of 2D Materials to Deep Sub-Ångström Resolution. *Nature* 2018, 559, 343–349. https://doi.org/10.1038/s41586-018-0298-5.
- (39) Komsa, H.-P.; Kotakoski, J.; Kurasch, S.; Lehtinen, O.; Kaiser, U.; Krasheninnikov, A. V. Two-Dimensional Transition Metal Dichalcogenides under Electron Irradiation: Defect Production and Doping. *Phys. Rev. Lett.* **2012**, *109*, 035503. https://doi.org/10.1103/PhysRevLett.109.035503.
- (40) Parkin, W. M.; Balan, A.; Liang, L.; Das, P. M.; Lamparski, M.; Naylor, C. H.; Rodríguez-Manzo, J. A.; Johnson, A. T. C.; Meunier, V.; Drndić, M. Raman Shifts in Electron-Irradiated Monolayer MoS ₂. *ACS Nano* **2016**, *10* (4), 4134–4142. https://doi.org/10.1021/acsnano.5b07388.
- (41) Wang, S.; Li, H.; Sawada, H.; Allen, C. S.; Kirkland, A. I.; Grossman, J. C.; Warner, J. H. Atomic Structure and Formation Mechanism of Sub-Nanometer Pores in 2D Monolayer MoS ₂. *Nanoscale* **2017**, *9* (19), 6417–6426. https://doi.org/10.1039/C7NR01127J.
- (42) Masih Das, P.; Danda, G.; Cupo, A.; Parkin, W. M.; Liang, L.; Kharche, N.; Ling, X.; Huang, S.; Dresselhaus, M. S.; Meunier, V.; Drndić, M. Controlled Sculpture of Black Phosphorus Nanoribbons. *ACS Nano* **2016**, *10* (6), 5687–5695. https://doi.org/10.1021/acsnano.6b02435.
- (43) Masih Das, P.; Thiruraman, J. P.; Zhao, M.; Mandyam, S.; Johnson, A. T. C.; Drndic, M. Atomic-Scale Patterning in Two-Dimensional van Der Waals Superlattices. *Nanotechnology* **2019**. https://doi.org/10.1088/1361-6528/ab596c.
- (44) Masih Das, P.; Drndić, M. *In Situ* 2D MoS ₂ Field-Effect Transistors with an Electron Beam Gate. *ACS Nano* **2020**, *14* (6), 7389–7397. https://doi.org/10.1021/acsnano.0c02908.
- (45) Danda, G.; Masih Das, P.; Chou, Y.-C.; Mlack, J. T.; Parkin, W. M.; Naylor, C. H.; Fujisawa, K.; Zhang, T.; Fulton, L. B.; Terrones, M.; Johnson, A. T. C.; Drndić, M. Monolayer WS₂ Nanopores for DNA Translocation with Light-Adjustable Sizes. *ACS Nano* **2017**, *11* (2), 1937–1945. https://doi.org/10.1021/acsnano.6b08028.
- (46) Algara-Siller, G.; Kurasch, S.; Sedighi, M.; Lehtinen, O.; Kaiser, U. The Pristine Atomic Structure of MoS2 Monolayer Protected from Electron Radiation Damage by Graphene. *Applied Physics Letters* **2013**, *103* (20). https://doi.org/10.1063/1.4830036.
- (47) Yoshimura, A.; Lamparski, M.; Kharche, N.; Meunier, V. First-Principles Simulation of Local Response in Transition Metal Dichalcogenides under Electron Irradiation. *Nanoscale* **2018**, *10*, 2388–2397. https://doi.org/10.1039/C7NR07024A.
- (48) Zan, R.; Ramasse, Q. M.; Jalil, R.; Georgiou, T.; Bangert, U.; Novoselov, K. S. Control of Radiation Damage in MoS2 by Graphene Encapsulation. *ACS Nano* **2013**, *7* (11), 10167–10174. https://doi.org/10.1021/nn4044035.
- (49) Danda, G.; Masih Das, P.; Drndic, M. Laser-Induced Fabrication of Nanoporous Monolayer WS2 Membranes. *2D Materials* **2018**, *5* (3), 035011.
- (50) Wen, Y.; Ophus, C.; Allen, C. S.; Fang, S.; Chen, J.; Kaxiras, E.; Kirkland, A. I.; Warner, J. H. Simultaneous Identification of Low and High Atomic Number Atoms in Monolayer 2D Materials Using 4D Scanning Transmission Electron Microscopy. *Nano Lett.* **2019**, *19* (9), 6482–6491. https://doi.org/10.1021/acs.nanolett.9b02717.
- (51) Suk, M. E.; Aluru, N. R. Ion Transport in Sub-5-Nm Graphene Nanopores. *The Journal of Chemical Physics* **2014**, *140* (8), 084707. https://doi.org/10.1063/1.4866643.
- (52) Aryal, P.; Sansom, M. S. P.; Tucker, S. J. Hydrophobic Gating in Ion Channels. *Journal of Molecular Biology* **2015**, *427* (1), 121–130. https://doi.org/10.1016/j.jmb.2014.07.030.
- (53) Jensen, M. O.; Borhani, D. W.; Lindorff-Larsen, K.; Maragakis, P.; Jogini, V.; Eastwood, M. P.; Dror, R. O.; Shaw, D. E. Principles of Conduction and Hydrophobic Gating in K+ Channels. Proceedings of the National Academy of Sciences 2010, 107 (13), 5833–5838. https://doi.org/10.1073/pnas.0911691107.
- (54) Roth, R.; Gillespie, D.; Nonner, W.; Eisenberg, R. E. Bubbles, Gating, and Anesthetics in Ion Channels. *Biophysical Journal* **2008**, *94* (11), 4282–4298. https://doi.org/10.1529/biophysj.107.120493.

- (55) Marion, S.; Macha, M.; Davis, S. J.; Chernev, A.; Radenovic, A. Wetting of Nanopores Probed with Pressure. *arXiv*:1911.05229 **2020**.
- (56) Krems, M.; Pershin, Y. V.; Di Ventra, M. Ionic Memcapacitive Effects in Nanopores. *Nano Lett.* **2010**, *10* (7), 2674–2678. https://doi.org/10.1021/nl1014734.
- (57) Tabard-Cossa, V. Instrumentation for Low-Noise High-Bandwidth Nanopore Recording. *Engineered Nanopores for Bioanalytical Applications: A Volume in Micro and Nano Technologies* **2013**, 59–93. https://doi.org/10.1016/B978-1-4377-3473-7.00003-0.
- (58) Smeets, R. M. M.; Keyser, U. F.; Dekker, N. H.; Dekker, C. (CUL-ID:3077100) Noise in Solid-State Nanopores. *Proceedings of the National Academy of Sciences of the United States of America* **2008**, *105* (2), 417–421. https://doi.org/10.1073/pnas.0705349105.
- (59) Zhang, Z. Y.; Deng, Y. S.; Tian, H. B.; Yan, H.; Cui, H. L.; Wang, D. Q. Noise Analysis of Monolayer Graphene Nanopores. *International Journal of Molecular Sciences* **2018**, *19* (9), 1–11. https://doi.org/10.3390/ijms19092639.
- (60) Chou, Y.-C.; Masih Das, P.; Monos, D. S.; Drndić, M. Lifetime and Stability of Silicon Nitride Nanopores and Nanopore Arrays for Ionic Measurements. ACS Nano 2020, a-n. https://doi.org/10.1021/acsnano.9b09964.
- (61) Hille, B. Pharmacological Modifications of the Sodium Channels of Frog Nerve. *The Journal of General Physiology* **1968**, *51* (2), 199–219. https://doi.org/10.1085/jgp.51.2.199.
- (62) Albrecht, T.; Gibb, T.; Nuttall, P. *Ion Transport in Nanopores*, First Edit.; Elsevier Inc., 2013. https://doi.org/10.1016/B978-1-4377-3473-7.00001-7.
- (63) Albrecht, T.; Gibb, T.; Nuttall, P. Ion Transport in Nanopores. In *Engineered Nanopores for Bioanalytical Applications*; Elsevier, 2013; pp 1–30. https://doi.org/10.1016/B978-1-4377-3473-7.00001-7.
- (64) Richards, L. A.; Richards, B. S.; Corry, B.; Schäfer, A. I. Experimental Energy Barriers to Anions Transporting through Nanofiltration Membranes. *Environmental Science and Technology* **2013**, *47* (4), 1968–1976. https://doi.org/10.1021/es303925r.
- (65) Venta, K. E.; Zanjani, M. B.; Ye, X.; Danda, G.; Murray, C. B.; Lukes, J. R.; Drndić, M. Gold Nanorod Translocations and Charge Measurement through Solid-State Nanopores. *Nano Lett.* 2014, 14 (9), 5358–5364. https://doi.org/10.1021/nl502448s.
- (66) Stein, D.; Kruithof, M.; Dekker, C. Surface-Charge-Governed Ion Transport in Nanofluidic Channels. *Phys. Rev. Lett.* **2004**, *93* (3), 035901. https://doi.org/10.1103/PhysRevLett.93.035901.
- (67) Balan, A.; Chien, C.-C.; Engelke, R.; Drndić, M. Suspended Solid-State Membranes on Glass Chips with Sub 1-PF Capacitance for Biomolecule Sensing Applications. *Sci Rep* **2016**, *5* (1), 17775. https://doi.org/10.1038/srep17775.
- (68) Balan, A.; Drndic, M. ULTRALOW CAPACITANCEGLASS SUPPORTED DIELECTRIC MEMBRANES FORMACROMOLECULAR ANALYSIS. US2017/0254796A1, September 7, 2017.
- (69) Hartel, A. J. W.; Shekar, S.; Ong, P.; Schroeder, I.; Thiel, G.; Shepard, K. L. High Bandwidth Approaches in Nanopore and Ion Channel Recordings A Tutorial Review. *Analytica Chimica Acta* **2019**, *1061*, 13–27. https://doi.org/10.1016/j.aca.2019.01.034.
- (70) Shekar, S.; Chien, C.-C.; Hartel, A.; Ong, P.; Clarke, O. B.; Marks, A.; Drndic, M.; Shepard, K. L. Wavelet Denoising of High-Bandwidth Nanopore and Ion-Channel Signals. *Nano Lett.* **2019**, *19* (2), 1090–1097. https://doi.org/10.1021/acs.nanolett.8b04388.
- (71) Hartel, A. J. W.; Ong, P.; Schroeder, I.; Giese, M. H.; Shekar, S.; Clarke, O. B.; Zalk, R.; Marks, A. R.; Hendrickson, W. A.; Shepard, K. L. Single-Channel Recordings of RyR1 at Microsecond Resolution in CMOS-Suspended Membranes. *Proc Natl Acad Sci USA* 2018, *115* (8), E1789–E1798. https://doi.org/10.1073/pnas.1712313115.
- (72) Chien, C.-C.; Shekar, S.; Niedzwiecki, D. J.; Shepard, K. L.; Drndić, M. Single-Stranded DNA Translocation Recordings through Solid-State Nanopores on Glass Chips at 10 MHz Measurement Bandwidth. *ACS Nano* **2019**, *13* (9), 10545–10554. https://doi.org/10.1021/acsnano.9b04626.
- (73) Besteman, K.; Zevenbergen, M. A. G.; Lemay, S. G. Charge Inversion by Multivalent Ions: Dependence on Dielectric Constant and Surface-Charge Density. *Physical Review E Statistical*,

- *Nonlinear, and Soft Matter Physics* **2005**, *72* (6), 1–9. https://doi.org/10.1103/PhysRevE.72.061501.
- (74) Healy, K.; Ray, V.; Willis, L. J.; Peterman, N.; Bartel, J.; Drndić, M. Fabrication and Characterization of Nanopores with Insulated Transverse Nanoelectrodes for DNA Sensing in Salt Solution. *Electrophoresis* **2012**, *33* (23), 3488–3496. https://doi.org/10.1002/elps.201200350.
- (75) Venta, K.; Shemer, G.; Puster, M.; Rodríguez-Manzo, J. A.; Balan, A.; Rosenstein, J. K.; Shepard, K.; Drndić, M. Differentiation of Short, Single-Stranded DNA Homopolymers in Solid-State Nanopores. *ACS Nano* **2013**, 7 (5), 4629–4636. https://doi.org/10.1021/nn4014388.

Table of Contents Graphic

